Accepted for publication in *Computers and Structures* on 10/10/16.
DOI: http: //dx.doi.org/10.1016/j.compstruc.2016.10.016

A novel 'boundary layer' finite element for the efficient analysis of thin cylindrical shells

Adrien Boyez[1], Adam J. Sadowski[2] & Bassam A. Izzuddin[3]

Abstract

Classical shell finite elements usually employ low-order polynomial shape functions to interpolate between nodal displacement and rotational degrees of freedom. Consequently, carefully-designed fine meshes are often required to accurately capture regions of high local curvature, such as at the 'boundary layer' of bending that occurs in cylindrical shells near a boundary or discontinuity. This significantly increases the computational cost of any analysis.

This paper is a 'proof of concept' illustration of a novel cylindrical axisymmetric shell element that is enriched with rigorously-derived transcendental shape functions to exactly capture the bending boundary layer. When complemented with simple polynomials to express the membrane displacements, a single boundary layer shell element is able to support very complex displacement and stress fields that are exact for distributed element loads of up to second order. A single element is usually sufficient per shell segment in a multi-strake shell.

The predictions of the novel element are compared against analytical solutions, a classical axisymmetric shell element with polynomial shape functions and the ABAQUS S4R shell element in three problems of increasing complexity and practical relevance. The element displays excellent numerical results with only a fraction of the total degrees of freedom and involves virtually no mesh design. The shell theory employed at present is kept deliberately simple for illustration purposes, though the formulation will be extended in future work.

Keywords

Thin cylindrical shell; axisymmetric shell; bending boundary layer; membrane action; finite element method; static condensation.

[1]PhD Student, Department of Civil & Environmental Engineering, Imperial College London
[2]Lecturer, Department of Civil & Environmental Engineering, Imperial College London
[3]Professor, Department of Civil & Environmental Engineering, Imperial College London

1. Introduction

Membrane action is the preferred load-carrying mechanism for shells, enabling efficient and economical use of material. As membrane forces can be obtained easily through equilibrium alone and are valid throughout much of the shell, membrane theory often forms the basis of design. However, bending action must be considered to fully take into account the effect of kinematic boundary conditions and to identify the range of validity of membrane action [1, 2]. Bending theory is significantly more complex mathematically, and even the very simplest linear axisymmetric variant requires the solution of a fourth-order non-homogeneous differential equation [3-6]. The high order of the governing equations belies a rich set of underlying physical behaviours, chief among them being the possibility of displacements and stress fields exhibiting rapid variations and high magnitudes near boundaries or discontinuities. This 'boundary layer' decays exponentially away from boundaries at a rate governed by the bending half-wavelength λ, settling on a particular integral corresponding to membrane action [2].

As analytical solutions cannot easily be obtained even for simple shell bending problems [2, 6-10], the finite element method (FEM) is widely employed instead [11-15]. Numerous shell element formulations exist, all based on polynomial shape functions of varying order. Membrane action is very 'smooth' and easily captured, but convergence to the solution in the vicinity of a bending boundary layer requires careful local mesh refinement [2, 15, 16]. Multi-segment or multi-strake shells may exhibit several boundary layers, each requiring a locally-refined interpolation field and contributing greatly to the total number of degrees of freedom in the system. For this reason, symmetry is exploited wherever possible for computational efficiency, although even axisymmetric shells exhibit boundary layers.

2. Scope of the study

The central concept behind the present study is to formally distinguish between membrane and bending components of the displacement solution at the level of the interpolation field, and to enrich the field through specialised bending shape functions derived rigorously from the governing differential equation. In this way the boundary layer is included natively within the finite element, leading to significant gains in accuracy and substantial economies in terms of total degrees of freedom, modelling effort and mesh design. The idea of enriching the interpolation field to account for specific local and global phenomena is not new and is the basis of the eXtended or General FEM (XFEM or GFEM) methods [17-20], but to the authors' knowledge it is the first time that such an approach has been applied to shell elements specifically to account for localised bending phenomena. The complexity is purposefully limited here to the very minimum required to demonstrate the validity of the approach: the proposed Cylindrical Shell Boundary Layer (CSBL) element currently supports linear stress analysis of axisymmetric loading on thin cylindrical shells, based on a simple Kirchoff-Love shell bending theory [21, 22]. However the use of a general constitutive relation enables the study of isotropic, uniformly orthotropic and meridionally-stiffened 'smeared' shells [22-24], making it an efficient tool for the axisymmetric bending stress analysis of multi-segment cylinders, silos, tanks and pressure vessels even in its present form. The performance of the linear CSBL element is illustrated on three example problems of increasing complexity, two of which relate directly to non-trivial practical axisymmetric design problems.

3. Axisymmetric bending theory for thin orthotropic cylindrical shells

The idea of using specialised shape functions to capture the boundary layer specifically in cylindrical shells stems directly from an analytical result in classical shell bending theory. Here, the mathematical distinction between the homogeneous and particular solutions of the governing differential equation corresponds directly to physical bending and membrane action respectively. The kinematic relations are kept linear in what follows, as even a simple axisymmetric thin-walled shell theory based on the Kirchhoff-Love assumptions [7, 21] captures the mechanics of meridional bending together with its associated boundary layer. This has the additional benefit that the solutions for the normal w and meridional u displacements are decoupled, permitting the origin of the proposed shape functions to be illustrated clearly. However, the linear constitutive relations are generalised to allow for the study of both isotropic and uniformly orthotropic cylinders via the 'smeared' stiffness approach [23, 24]. Lastly, as the transcendental bending shape functions of the proposed CSBL element are obtained directly from the analytical solution to the governing differential equation, some level of detail in presenting its derivation, however classical, is necessary here.

Under axisymmetric conditions, a cylindrical shell of radius r and thickness t may be subject to pressure loading normal p_n and meridionally tangential p_z to the midsurface (dimensions of [F.L^{-2}], as shown in Fig. 1. Axisymmetry of the loading, boundary conditions and geometry ensures that only five stress resultants act on the mid-surface of the thin shell: the meridional and circumferential membrane stress resultants n_z and n_θ ([F.L^{-1}]), the bending moment stress resultants m_z and m_θ ([FL.L^{-1}]), and the meridional transverse shear stress resultant q_z ([F.L^{-1}]). There are no displacements or gradients in the circumferential direction.

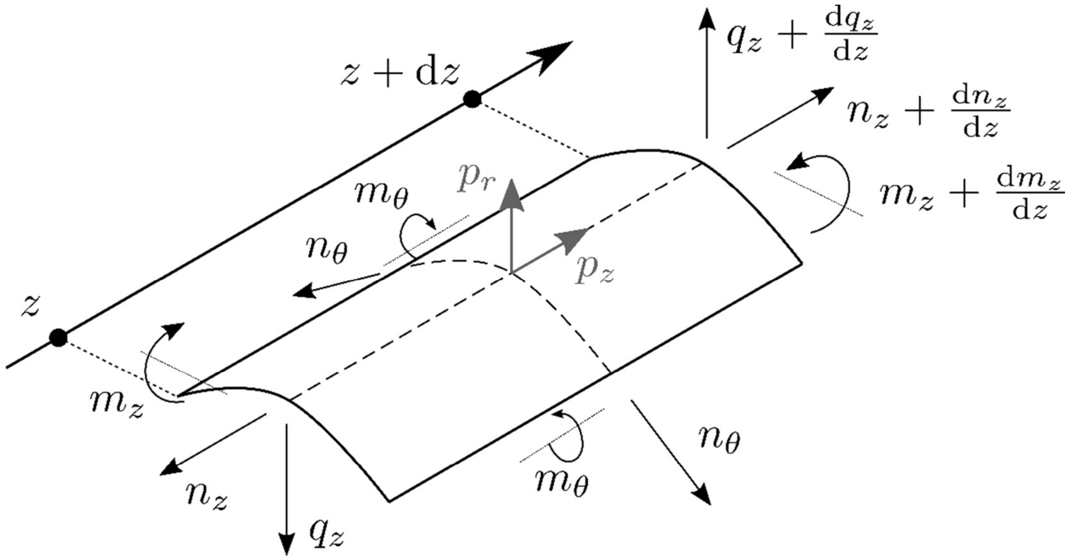

Fig. 1 – Equilibrium of an element of a thin-walled axisymmetric cylindrical shell

Considering equilibrium of an elementary cylinder section of length dz and arc length $rd\theta$ yields the following equations:

$$\frac{dn_z}{dz} = -p_z, \quad n_\theta = r\left(p_r + \frac{dq_z}{dz}\right) \text{ and } q_z = -\frac{dm_z}{dz} \tag{1}$$

The following constitutive and kinematic relations are used in this illustration [22]:

$$\begin{bmatrix} n_z \\ n_\theta \\ m_z \end{bmatrix} = \begin{bmatrix} C_{11} & C_{12} & C_{13} \\ C_{12} & C_{22} & 0 \\ C_{13} & 0 & C_{33} \end{bmatrix} \begin{bmatrix} \varepsilon_z \\ \varepsilon_\theta \\ \kappa_z \end{bmatrix} \text{ and } \begin{bmatrix} \varepsilon_z \\ \varepsilon_\theta \\ \kappa_z \end{bmatrix} = \begin{bmatrix} \frac{du}{dz} & \frac{w}{r} & \frac{d^2w}{dz^2} \end{bmatrix}^T \tag{2)(3}$$

where the C's represent appropriate stiffness coefficients that will be discussed later. The resultants m_θ and q_z need not be included in Eq. (2) as their corresponding generalised strains are zero. Combining Eqs. (1)-(3) and simplifying the result leads to a linear fourth-order ordinary differential equation in w only, the normal midsurface displacement:

$$\begin{aligned} & r\left(C_{11}C_{33} - C_{13}^2\right)\frac{d^4w}{dz^4} - 2C_{12}C_{13}\frac{d^2w}{dz^2} + \frac{1}{r}\left(C_{11}C_{22} - C_{12}^2\right)w = \ldots \\ & rC_{11}p_r + C_{12}\left(\int_0^z p_z dz - n_{z0}\right) + rC_{13}\frac{dp_z}{dz} \end{aligned} \tag{4}$$

Solving the homogeneous part of the equation requires finding the complex roots of the corresponding characteristic polynomial:

$$aX^4 + 2bX^2 + c = 0 \text{ where } \begin{cases} a = r\left(C_{11}C_{33} - C_{13}^2\right) \\ b = -C_{12}C_{13} \\ c = r^{-1}\left(C_{11}C_{22} - C_{12}^2\right) \end{cases} \tag{5}$$

Setting $Y = X^2$, this becomes a polynomial of second degree in Y, for which the discriminant is:

$$\delta = b^2 - ac = C_{12}^2 C_{13}^2 - (C_{11}C_{22} - C_{12}^2)(C_{11}C_{33} - C_{13}^2) \tag{6}$$

which is negative if and only if the following inequality is satisfied:

$$\frac{C_{12}^2}{C_{22}} + \frac{C_{13}^2}{C_{33}} < C_{11} \tag{7}$$

It is important to establish that this inequality will indeed always be satisfied, as this governs the functional form of the general solution to the homogeneous equation. For a very general uniformly orthotropic shell with elastic moduli E_z and E_θ, Poisson's ratio ν and thickness t, and 'smeared' meridional stiffeners of modulus E_s, cross-section area A_s, second moment of area I_s, spacing d_s and eccentricity e_s, the constitutive matrix **[C]** is the following [22]:

$$[\mathbf{C}] = \begin{bmatrix} \dfrac{E_z t}{1-\nu^2} + \dfrac{E_s A_s}{d_s} & \nu\dfrac{\sqrt{E_z E_\theta}\, t}{1-\nu^2} & \dfrac{e_s E_s A_s}{d_s} \\ \nu\dfrac{\sqrt{E_z E_\theta}\, t}{1-\nu^2} & \dfrac{E_\theta t}{1-\nu^2} & 0 \\ \dfrac{e_s E_s A_s}{d_s} & 0 & \dfrac{E_z t^3}{12\left(1-\nu^2\right)} + \dfrac{E_s I_s}{d_s} + \dfrac{e_s^2 E_s A_s}{d_s} \end{bmatrix} \tag{8}$$

The left-hand side of the inequality in Eq. (7) may be evaluated as:

$$\frac{C_{12}^2}{C_{22}} + \frac{C_{13}^2}{C_{33}} = \nu^2 \cdot \frac{E_z t}{1-\nu^2} + \frac{1}{1+k} \cdot \frac{E_s A_s}{d_s} \text{ where } k = \frac{E_z t^3 d_s}{12\left(1-\nu^2\right) e_s^2 E_s A_s} + \frac{I_s}{e_s^2 A_s} \tag{9}$$

But $\nu^2 < 1$ by definition, and since initial elastic stiffnesses and dimensions must always be positive it follows that $k > 0$ and thus $1 / (1+k) < 1$. Consequently:

$$\frac{C_{12}^2}{C_{22}} + \frac{C_{13}^2}{C_{33}} < \frac{E_z t}{1-\nu^2} + \frac{E_s A_s}{d_s} = C_{11} \tag{10}$$

Thus the inequality is always satisfied. Accordingly, the characteristic polynomial in Eq. (5) exhibits four complex roots and the general solution to the homogeneous equation may be expressed using exponential and trigonometric functions:

$$w_b(z) = \mathrm{e}^{\pi\frac{z}{\alpha}}\left[A_1\cos\pi\frac{z}{\beta} + A_2\cos\pi\frac{z}{\beta}\right] + \mathrm{e}^{-\pi\frac{z}{\alpha}}\left[A_3\cos\pi\frac{z}{\beta} + A_4\cos\pi\frac{z}{\beta}\right] \tag{11}$$

where A_i are integration constants depending on boundary conditions (four in total) and α and β are the linear meridional bending half-wavelengths:

$$\begin{cases} \alpha = \pi\sqrt{2r}\left(\sqrt{\dfrac{C_{11}C_{22}-C_{12}^2}{C_{11}C_{33}-C_{13}^2}} + \dfrac{C_{12}C_{13}}{C_{11}C_{33}-C_{13}^2}\right)^{-1/2} \\ \beta = \pi\sqrt{2r}\left(\sqrt{\dfrac{C_{11}C_{22}-C_{12}^2}{C_{11}C_{33}-C_{13}^2}} - \dfrac{C_{12}C_{13}}{C_{11}C_{33}-C_{13}^2}\right)^{-1/2} \end{cases} \tag{12}$$

The above equations fully govern the extent of the bending component of w and thus of the boundary layer, and for this reason the notation w_b has been used. The two bending half-wavelengths in particular contain information about the rate of decay of the boundary layer in a shell segment and play a key role in what follows. They are identical for an unstiffened shell where there is no coupling between the meridional membrane stress resultant n_z and curvature κ_z ($C_{13} = 0$), in which case they are both denoted by the more familiar symbol λ:

$$\lambda = \alpha = \beta = \pi\sqrt{2r}\left(\frac{C_{11}C_{33}}{C_{11}C_{22}-C_{12}^2}\right)^{1/4} \tag{13}$$

Introducing the following convenient short-hand notation

$$\omega_\alpha = \frac{\pi}{\alpha} \quad \omega_\beta = \frac{\pi}{\beta} \quad \mathrm{exc}^{\pm}(z) = \exp(\pm\omega_\alpha z)\cos(\omega_\beta z) \quad \mathrm{exs}^{\pm}(z) = \exp(\pm\omega_\alpha z)\sin(\omega_\beta z) \tag{14}$$

permits w_b to be written in a more compact form:

$$w_b(z) = A_1\,\mathrm{exc}^-(z) + A_2\,\mathrm{exs}^-(z) + A_3\,\mathrm{exc}^+(z) + A_4\,\mathrm{exs}^+(z) \tag{15}$$

The particular solution w_m governing the membrane component of w, or the normal displacement that would exist if bending effects were ignored, is classically obtained by neglecting all derivatives in Eq. (4):

$$w_m = \frac{r}{C_{11}C_{22}-C_{12}^2}\left[rC_{11}p_r + C_{12}\left(\int_0^z p_z\,\mathrm{d}z - n_{z0}\right) + rC_{13}\frac{\mathrm{d}p_z}{\mathrm{d}z}\right] \tag{16}$$

where n_{z0} is a prescribed meridional 'edge' load. The total normal displacement w is then simply obtained by superposition: $w = w_b + w_m$. Lastly, the meridional displacement u may be obtained by integrating the following intermediate result:

$$C_{11}\frac{\mathrm{d}u}{\mathrm{d}z} = \left(\int_0^z -p_z \mathrm{d}z + n_{z0}\right) - C_{12}\frac{w}{r} - C_{13}\frac{\mathrm{d}^2 w}{\mathrm{d}z^2} \tag{17}$$

It may be shown that u may similarly be decomposed into components associated with bending u_b (Eq. (18)) and membrane u_m (Eq. (19)) actions only:

$$\begin{aligned} u_b = \frac{-C_{12}}{rC_{11}(\omega_\alpha{}^2 + \omega_\beta{}^2)} & \big[(-\omega_\alpha A_1 - \omega_\beta A_2) exc^- z + (\omega_\beta A_1 - \omega_\alpha A_2) exs^- z \\ & + (\omega_\alpha A_3 - \omega_\beta A_4) exc^+ z + (\omega_\beta A_3 + \omega_\alpha A_4) exs^+ z\big] \\ - \frac{C_{13}}{C_{11}} & \big[(-\omega_\alpha A_1 + \omega_\beta A_2) exc^- z + (-\omega_\beta A_1 - \omega_\alpha A_2) exs^- z \\ & + (\omega_\alpha A_3 + \omega_\beta A_4) exc^+ z + (-\omega_\beta A_3 + \omega_\alpha A_4) exs^+ z\big] \end{aligned} \tag{18}$$

$$\begin{aligned} u_m = & \frac{1}{C_{11}C_{22} - C_{12}{}^2}\left[-rC_{12}\int_0^z p_r \mathrm{d}z + C_{22}\left(-\int_0^z\left(\int_0^z p_z\ \mathrm{d}z\right)\mathrm{d}z + n_{z0}z\right)\right] + u_0 \\ & - \frac{rC_{13}}{C_{11}C_{22} - C_{12}{}^2}\left[r\frac{\mathrm{d}p_r}{\mathrm{d}z} + 2\frac{C_{12}}{C_{11}}p_z + r\frac{C_{13}}{C_{11}}\frac{\mathrm{d}^2 p_r}{\mathrm{d}z^2}\right] \end{aligned} \tag{19}$$

where u_0 is a prescribed meridional displacement. While it is perhaps not obvious, closer inspection shows that u_b shares the same functional form with w_b and is governed by the same bending half-wavelengths α and β.

4. The axisymmetric cylindrical shell boundary layer (CSBL) element

It is worth briefly reflecting that the expressions for w_m and u_m (Eqs. (16) and (19)) feature the distributed loads p_n and p_z whereas those of w_b and u_b (Eqs. (15) and (18)) do not, while the converse is true for the integration constants A_1 to A_4. The membrane component of the solution thus alone equilibrates the applied loads, while the bending component alone satisfies kinematic boundary conditions. These mechanisms are independent both mathematically and physically, a distinction that leads logically to the idea of treating w_b, u_b, w_m and u_m as independent variables in a shell finite element formulation, with shape functions tailored to best capture each underlying physical mechanism. The authors are not aware of a similar approach having been implemented in any widely-used shell element.

4.1. Bending shape functions

A set of unique shape functions G_1 to G_4 may be obtained by reformulating w_b (Eq. (15)) using a different base, so that the unknown integration constants A_1, A_2, A_3 and A_4 are expressed instead in terms of unknown displacements and rotations at each end of the cylinder (defined without loss of generality at $z = 0$ and h), namely $w_{b1} = w_b(0)$, $\theta_{b1} = w'_b(0)$, $w_{b2} = w_b(h)$ and $\theta_{b2} = w'_b(h)$. These are then the nodal degrees of freedom (DOFs) corresponding specifically to the bending component of the normal displacement w_b.

$$\underbrace{\begin{Bmatrix} \mathrm{exc}^- \\ \mathrm{exs}^- \\ \mathrm{exc}^+ \\ \mathrm{exs}^+ \end{Bmatrix}^{\mathrm{T}}}_{\{\mathbf{F}\}^{\mathrm{T}}} \underbrace{\begin{Bmatrix} A_1 \\ A_2 \\ A_3 \\ A_4 \end{Bmatrix}}_{\{\mathbf{A}\}} = \underbrace{\begin{Bmatrix} G_1 \\ G_2 \\ G_3 \\ G_4 \end{Bmatrix}^{\mathrm{T}}}_{\{\mathbf{G}\}^{\mathrm{T}}} \underbrace{\begin{Bmatrix} w_{b1} \\ \theta_{b1} \\ w_{b2} \\ \theta_{b2} \end{Bmatrix}}_{\{\mathbf{W}_b\}} \tag{20}$$

The vector $\{\mathbf{W}_b\}$ is expressed in terms of the constants A_i using Eq. (15) as follows:

$$\underbrace{\begin{Bmatrix} w_{b1} \\ \theta_{b1} \\ w_{b2} \\ \theta_{b2} \end{Bmatrix}}_{\{\mathbf{W}_b\}} = \underbrace{\begin{bmatrix} \mathrm{exc}^-(0) & \mathrm{exs}^-(0) & \mathrm{exc}^+(0) & \mathrm{exs}^+(0) \\ (\mathrm{exc}^-)'(0) & (\mathrm{exs}^-)'(0) & (\mathrm{exc}^+)'(0) & (\mathrm{exs}^+)'(0) \\ \mathrm{exc}^-(h) & \mathrm{exs}^-(h) & \mathrm{exc}^+(h) & \mathrm{exs}^+(h) \\ (\mathrm{exc}^-)'(h) & (\mathrm{exs}^-)'(h) & (\mathrm{exc}^+)'(h) & (\mathrm{exs}^+)'(h) \end{bmatrix}}_{[\mathbf{T}]} \underbrace{\begin{Bmatrix} A_1 \\ A_2 \\ A_3 \\ A_4 \end{Bmatrix}}_{\{\mathbf{A}\}} \tag{21}$$

Introducing Eq. (21) into Eq. (20) leads to a linear system that is easily inverted to obtain the transcendental G_i functions in closed form:

$$\{\mathbf{G}\}^{\mathrm{T}}[\mathbf{T}]\{\mathbf{A}\} = \{\mathbf{F}\}^{\mathrm{T}}\{\mathbf{A}\} \quad \Rightarrow \quad \{\mathbf{G}\} = [\mathbf{g}]\{\mathbf{F}\} \quad \text{where} \quad [\mathbf{g}] = \left([\mathbf{T}]^{-1}\right)^{\mathrm{T}} \tag{22}$$

or written out in full:

$$\begin{Bmatrix} G_1 \\ G_2 \\ G_3 \\ G_4 \end{Bmatrix} = \begin{bmatrix} g_{11} & g_{12} & g_{13} & g_{14} \\ g_{21} & g_{22} & g_{23} & g_{24} \\ g_{31} & g_{32} & g_{33} & g_{34} \\ g_{41} & g_{42} & g_{43} & g_{44} \end{bmatrix} \begin{Bmatrix} \mathrm{exc}^- \\ \mathrm{exs}^- \\ \mathrm{exc}^+ \\ \mathrm{exs}^+ \end{Bmatrix} \tag{23}$$

Since $[\mathbf{g}]$ is obtained by inversion and transposition of $[\mathbf{T}]$, its terms share a common denominator d that is the determinant of $[\mathbf{T}]$:

$$\begin{aligned} d &= -\left(2\sin(\omega_\beta h)\right)^2 \omega_\alpha^2 + \left(2\sinh(\omega_\alpha h)\right)^2 \omega_\beta^2 \\ &= 4\left(\omega_\beta \sinh(\omega_\alpha h) - \omega_\alpha \sin(\omega_\beta h)\right)\left(\omega_\beta \sinh(\omega_\alpha h) + \omega_\alpha \sin(\omega_\beta h)\right) \end{aligned} \tag{24}$$

This determinant is zero if and only if either bending half-wavelength α or β is zero, which cannot happen for physical shells, so the resulting G_i functions are always well-defined. The individual g_{ii} terms, all scalars, are given by:

$$
\begin{aligned}
d \cdot g_{11} &= \left(-2\sin_h^2\right) \omega_\alpha^2 + \left(2\cos_h \sin_h\right) \omega_\alpha\omega_\beta + \left(\mathrm{e}_h^2 - 1\right) \omega_\beta^2 \\
d \cdot g_{12} &= \left(2\cos_h \sin_h\right) \omega_\alpha^2 + \left(\mathrm{e}_h^2 + 1 - 2\cos_h^2\right) \omega_\alpha\omega_\beta \\
d \cdot g_{13} &= \left(-2\sin_h^2\right) \omega_\alpha^2 + \left(-2\cos_h \sin_h\right) \omega_\alpha\omega_\beta + \left(\mathrm{e}_h^{-2} - 1\right) \omega_\beta^2 \\
d \cdot g_{14} &= \left(2\cos_h \sin_h\right) \omega_\alpha^2 + \left(-\mathrm{e}_h^{-2} - 1 + 2\cos_h^2\right) \omega_\alpha\omega_\beta
\end{aligned}
\tag{25}
$$

$$
\begin{aligned}
d \cdot g_{21} &= \left(2\sin_h^2\right) \omega_\alpha \\
d \cdot g_{22} &= \left(-2\cos_h \sin_h\right) \omega_\alpha + \left(\mathrm{e}_h^2 - 1\right) \omega_\beta \\
d \cdot g_{23} &= \left(-2\sin_h^2\right) \omega_\alpha \\
d \cdot g_{24} &= \left(2\cos_h \sin_h\right) \omega_\alpha + \left(\mathrm{e}_h^{-2} - 1\right) \omega_\beta
\end{aligned}
\tag{26}
$$

$$
\begin{aligned}
d \cdot g_{31} &= \left(-2\sinh_h \cos_h\right) \omega_\beta^2 + \left(-2\cosh_h \sin_h\right) \omega_\alpha\omega_\beta \\
d \cdot g_{32} &= \left(-2\sinh_h \sin_h\right) \omega_\beta^2 + \left(-2\sinh_h \cos_h\right) \omega_\alpha\omega_\beta + \left(-2\mathrm{e}_h \sin_h\right) \omega_\alpha^2 \\
d \cdot g_{33} &= \left(2\sinh_h \cos_h\right) \omega_\beta^2 + \left(2\cosh_h \sin_h\right) \omega_\alpha\omega_\beta \\
d \cdot g_{34} &= \left(2\sinh_h \sin_h\right) \omega_\beta^2 + \left(-2\sinh_h \cos_h\right) \omega_\alpha\omega_\beta + \left(-2\mathrm{e}_h^{-1} \sin_h\right) \omega_\alpha^2
\end{aligned}
\tag{27}
$$

$$
\begin{aligned}
d \cdot g_{41} &= \left(2\sinh_h \sin_h\right) \omega_\beta \\
d \cdot g_{42} &= \left(-2\sinh_h \cos_h\right) \omega_\beta + \left(2\mathrm{e}_h \sin_h\right) \omega_\alpha \\
d \cdot g_{43} &= \left(-2\sinh_h \sin_h\right) \omega_\beta \\
d \cdot g_{44} &= \left(2\sinh_h \cos_h\right) \omega_\beta + \left(-2\mathrm{e}_h^{-1} \sin_h\right) \omega_\alpha
\end{aligned}
\tag{28}
$$

where, for compactness, the following additional notation was employed:

$$
\mathrm{e}_h = \exp(\omega_\alpha h) \qquad
\begin{aligned}
\cosh_h &= \cosh(\omega_\alpha h) & \cos_h &= \cos(\omega_\beta h) \\
\sinh_h &= \sinh(\omega_\alpha h) & \sin_h &= \sin(\omega_\beta h)
\end{aligned}
\tag{29}
$$

Although the symmetry may not be obvious from the g_{ii} terms, it can easily be shown that $G_3(z) = G_1(h - z)$ and $G_4(z) = -G_2(h - z)$. The four G_i functions are illustrated in Fig. 2 for isotropic ($\lambda = \alpha = \beta$) cylindrical elements of three different lengths h relative to λ. Fig. 2a shows $h/\lambda = 5$ where the total element length is significantly greater than the width of the boundary layer, and the associated bending deformations are localised near either node. Fig. 2b shows a shorter cylinder with $h/\lambda = 2$, where neither boundary layer has enough width to decay and one begins to infringe on the other, while Fig. 2c shows a very short cylinder with $h/\lambda = ½$ where two boundary layers overlap entirely. The bending half-wavelength λ (or α and β) contains the entirety of the information about the rate of decay of the boundary layer, and as it is always known *a priori* for each element under linear conditions, the need for local refinement of the interpolating field and its associated degree of freedom cost are eliminated. Lastly, an interesting property of the G_i functions seen in Fig. 2d is their convergence to the well-known Hermite cubic functions (N_i in Table 1) as $\lambda \to \infty$ or $h/\lambda \to 0$, easily verified through an analytical Taylor series expansion. It should come as no surprise that structures for which the primary load carrying mechanism is transverse bending (e.g. beams and plates) actually exhibit an infinite bending boundary layer.

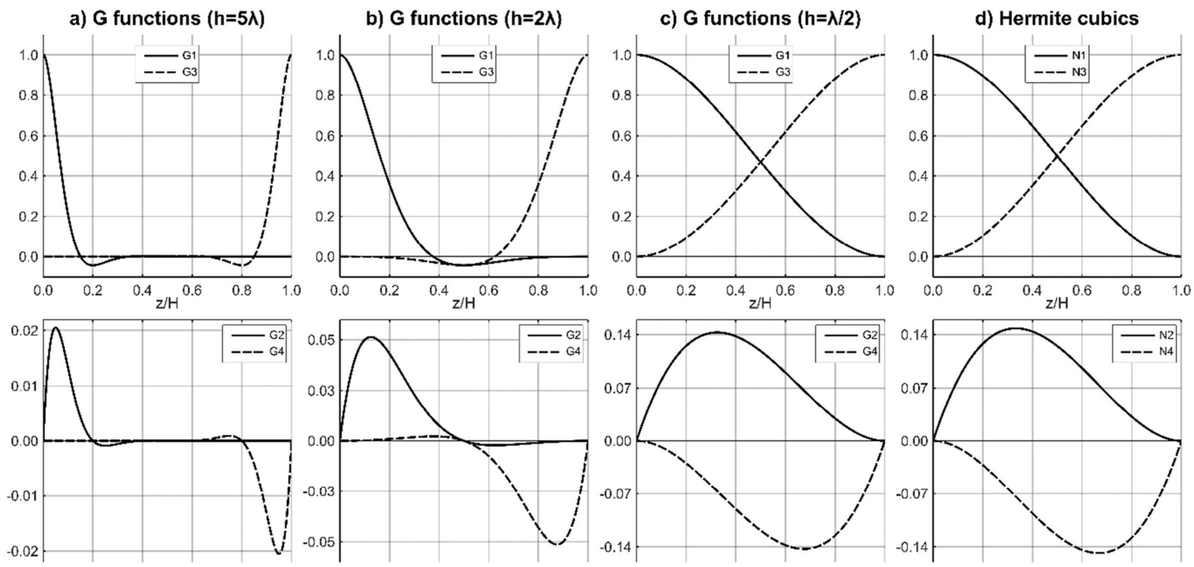

Fig. 2 – Illustration of bending 'boundary layer' shape functions for various h/λ ratios, and comparison with classical Hermite cubic polynomials

The bending component of the meridional displacement u_b (Eq. (18)) exhibits the same functional form as w_b (Eq. (15)) and is governed by the same bending half-wavelengths, so it is proposed that the same G functions may also be used for its interpolation. The associated nodal degrees of freedom are then $u_b = u_b(0)$, $u'_{b1} = u'_b(0)$, $u_{b2} = u_b(h)$and $u'_{b2} = u'_b(h)$, where u'_b is the tangent slope of u_b.

4.2. Membrane shape functions

While the functional form of the bending boundary layer may be determined uniquely from the kinematics, the same cannot be said for the membrane components of the displacements as these depend on the distribution of the loading which can be arbitrary. The CSBL element should be thought of as a high-order element, as it relies on higher-complexity shape functions rather than more elements (p-refinement over h-refinement [25]) to capture the bending boundary layer, and using polynomials of the lowest order to interpolate the membrane displacements would be somewhat in conflict with that purpose. The choice was therefore made to permit the membrane interpolation field to exactly accommodate distributed element loads p_n and p_z up to second-order polynomial variation with z. This permits an exact solution to the most common uniform and hydrostatic load cases, while more complex load cases can be approximated as piecewise-quadratic functions. As will be shown in what follows, many nonlinear load cases of practical importance are very smooth, such as the 'Janssen' silo pressure distribution [26], and are captured very well in this piecewise manner. Other choices for the membrane shape functions (higher order polynomials, or shape functions tailored for certain loads) are of course possible, but would result in a CSBL element with a higher internal DOF count, and should therefore be made only if the trade-off in terms of overall computational efficiency is deemed favourable.

Table 1 – Hermite cubics and other polynomial shape functions

$N_1 = 1 - 3\dfrac{z^2}{h^2} + 2\dfrac{z^3}{h^3}$	$N_2 = z - 2\dfrac{z^2}{h} + \dfrac{z^3}{h^2}$	$N_3 = 3\dfrac{z^2}{h^2} - 2\dfrac{z^3}{h^3}$	$N_4 = -\dfrac{z^2}{h} + \dfrac{z^3}{h^2}$
$L_1 = 1 - \dfrac{z}{h}$	$L_2 = \dfrac{z}{h}$	$P = 4\dfrac{z}{h}\left(1 - \dfrac{z}{h}\right)$	$C = 12\sqrt{3}\,\dfrac{z}{h}\left(1 - \dfrac{z}{h}\right)\left(\dfrac{1}{2} - \dfrac{z}{h}\right)$
$U = 1$	$L = -1 + 2\dfrac{z}{h}$		$Q = 16\left(\dfrac{z}{h}\right)^2\left(1 - \dfrac{z}{h}\right)^2$

Accordingly, Eqs (16) and (19) dictate that any shape functions for w_m and u_m must be a base for polynomials of at least order 3 and 4 respectively ($\mathbb{R}[3]$ and $\mathbb{R}[4]$). There are many ways to achieve this using functions presented in Table 1: a base for $\mathbb{R}[1]$ can be (L_1, L_2) or (U, L), both of which can be completed by (P), (P,C) or (P,C,Q) to form bases of $\mathbb{R}[2]$, $\mathbb{R}[3]$ and $\mathbb{R}[4]$ respectively. Alternatively, the classical Hermite cubics (N_1,N_2,N_3,N_4) form a base of $\mathbb{R}[3]$ that can also be completed by a quartic (Q) to reach the next order.

Apart from Q, each one of these functions features a non-zero slope or displacement at 0 or h, making them impractical for use as additional shape functions. Continuity of u, w and its first derivative θ is required between elements in order to ensure convergence with h-refinement, and if the polynomials from Table 1 were to be used, these continuity conditions would need to be enforced at the nodes using, for instance, Lagrange multipliers [12]. It is, however, possible to use these functions in conjunction with the previously-defined bending shape functions to create an interpolation field that has the appropriate number of nodal DOFs (giving the total value of u, w and θ at each node) while making all other DOFs element-specific, therefore allowing for efficient static condensation [13].

4.3. Element degrees of freedom

One option is to use the DOFs associated with the bending shape functions as the nodal DOFs, and to use additional element-specific DOFs with corresponding shape functions that linearly combine the bending shape functions with the chosen polynomials such that the end displacements are zero for u and both the end displacements and slopes are zero for w. This would lead to the following shape functions being used (the shape functions associated with a nodal DOF have a circumflex accent ^):

$$\text{For } u\text{: } \left(\hat{G}_1, G_2, \hat{G}_3, G_4, U^{\#}, L^{\#}, P, C, Q\right) \text{ with } \begin{cases} U^{\#} = U - G_1 - G_3 \\ L^{\#} = L + G_1 - G_3 \end{cases} \tag{30}$$

$$\text{For } w\text{: } \left(\hat{G}_1, \hat{G}_2, \hat{G}_3, \hat{G}_4, U^{\#}, L^{\#\sim}, P^{\sim}, C^{\sim}\right) \text{ with } \begin{cases} L^{\#\sim} = L^{\#} - (2/h)(G_2 + G_4) \\ P^{\sim} = P - (4/h)(G_2 - G_4) \\ C^{\sim} = C - \left(6\sqrt{3}/h\right)(G_2 + G_4) \end{cases} \tag{31}$$

Alternatively, DOFs associated with the Hermite cubics could be the nodal DOFs, and they could be combined with the bending shape functions to make them element-specific:

$$\text{For } u\text{: } \left(\hat{N}_1, N_2, \hat{N}_3, N_4, G_1^{\#}, G_2, G_3^{\#}, G_4, Q\right) \text{ with } \begin{cases} G_1^{\#} = G_1 - N_1 \\ G_3^{\#} = G_3 - N_3 \end{cases} \tag{32}$$

$$\text{For } w\text{: } \left(\hat{N}_1, \hat{N}_2, \hat{N}_3, \hat{N}_4, G_1^{\#}, G_2^{\sim}, G_3^{\#}, G_4^{\sim}\right) \text{ with } \begin{cases} G_2^{\sim} = G_2 - N_2 \\ G_4^{\sim} = G_4 - N_2 \end{cases} \tag{33}$$

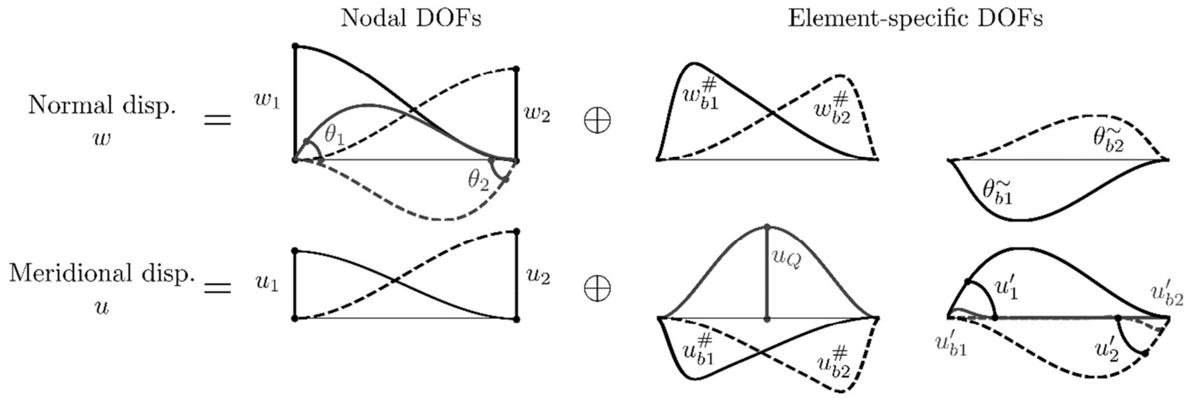

Fig. 3 – Nodal and element-specific DOFs for the 2-node axisymmetric CSBL element

Although both options are valid and interpolate the same displacement field from a mathematical point of view, the second one (illustrated in Fig. 3) is preferred computationally as it leads to a significantly simpler element stiffness matrix and equivalent load vector with 6 nodal DOFs ($w_1, \theta_1, u_1, w_2, \theta_2, u_2$) and 11 element-specific DOFs ($w_{b1}^{\#}, \theta_{b1}^{\sim}, w_{b2}^{\#}, \theta_{b2}^{\sim}, u'_1, u'_2, u_{b1}^{\#}, u'_{b1}, u_{b2}^{\#}, u'_{b2}, u_Q$). An interesting observation is that in the limit where $h/\lambda \rightarrow 0$, the convergence of the G functions to the Hermite cubics makes the shape functions $\left(G_1^{\#}, G_2^{\sim}, G_3^{\#}, G_4^{\sim}\right)$ tend to zero and their associated element-specific DOFs redundant, with only 3 element-specific DOFs (u'_1, u'_2, u_Q) remaining.

The following interpolation function $\{\mathbf{G}\}$ and DOF $\{\mathbf{d}\}$ vectors may now be defined at the element level:

$$
\begin{gathered}
\{\mathbf{G}\}_{17\times1} = \left\{\begin{array}{c}\mathbf{G}_w \\ \hdashline \mathbf{G}_u\end{array}\right\} \quad \text{and} \quad \{\mathbf{d}\}_{17\times1} = \left\{\begin{array}{c}\mathbf{d}_w \\ \hdashline \mathbf{d}_u\end{array}\right\} \\
\text{where} \quad \begin{aligned} \{\mathbf{G}_w\}_{8\times1} &= \begin{bmatrix} N_1 & N_2 & N_3 & N_4 & G_1^{\#} & G_2^{\sim} & G_3^{\#} & G_4^{\sim} \end{bmatrix}^{\mathbf{T}} \\ \{\mathbf{d}_w\}_{8\times1} &= \begin{bmatrix} w_1 & \theta_1 & w_2 & \theta_2 & w_{b1}^{\#} & \theta_{b1}^{\sim} & w_{b2}^{\#} & \theta_{b2}^{\sim} \end{bmatrix}^{\mathbf{T}} \end{aligned} \\
\text{and} \quad \begin{aligned} \{\mathbf{G}_u\}_{9\times1} &= \begin{bmatrix} N_1 & N_2 & N_3 & N_4 & G_1^{\#} & G_2 & G_3^{\#} & G_4 & Q \end{bmatrix}^{\mathbf{T}} \\ \{\mathbf{d}_u\}_{9\times1} &= \begin{bmatrix} u_1 & u'_1 & u_2 & u'_2 & u_{b1}^{\#} & u'_{b1} & u_{b2}^{\#} & u'_{b2} & u_Q \end{bmatrix}^{\mathbf{T}} \end{aligned}
\end{gathered}
\tag{34}
$$

Extraction matrices may be defined to obtain $\{\mathbf{G}_w\}$ and $\{\mathbf{G}_u\}$ from $\{\mathbf{G}\}$, as well as $\{\mathbf{d}_w\}$ and $\{\mathbf{d}_u\}$ from $\{\mathbf{d}\}$, respectively:

$$
\begin{aligned}
\{\mathbf{G}_w\}_{8\times1} &= [\mathbf{t}_w]_{8\times17}\{\mathbf{G}\}_{17\times1} \quad \text{and} \quad \{\mathbf{d}_w\}_{8\times1} = [\mathbf{t}_w]_{8\times17}\{\mathbf{d}\}_{17\times1} \\
\{\mathbf{G}_u\}_{9\times1} &= [\mathbf{t}_u]_{9\times17}\{\mathbf{G}\}_{17\times1} \quad \text{and} \quad \{\mathbf{d}_u\}_{9\times1} = [\mathbf{t}_u]_{9\times17}\{\mathbf{d}\}_{17\times1}
\end{aligned}
\tag{35}
$$

Therefore, displacements w and u can be obtained as a product of $\{\mathbf{G}\}$ and $\{\mathbf{d}\}$:

$$
\begin{aligned}
w &= \{\mathbf{G}_w\}^{\mathrm{T}}\{\mathbf{d}_w\} = \{\mathbf{G}\}^{\mathrm{T}}[\mathbf{t}_w]^{\mathrm{T}}[\mathbf{t}_w]\{\mathbf{d}\} = \{\mathbf{G}\}^{\mathrm{T}}[\mathbf{T}_w]\{\mathbf{d}\} \\
u &= \{\mathbf{G}_u\}^{\mathrm{T}}\{\mathbf{d}_u\} = \{\mathbf{G}\}^{\mathrm{T}}[\mathbf{t}_u]^{\mathrm{T}}[\mathbf{t}_u]\{\mathbf{d}\} = \{\mathbf{G}\}^{\mathrm{T}}[\mathbf{T}_u]\{\mathbf{d}\}
\end{aligned}
\tag{36}
$$

4.4. Strain energy and element stiffness matrix

The strain energy $\mathscr{E}$ may be obtained in the classical manner as a double integral over the cylinder (simplifying to a single integral along the meridian due to axisymmetry) incorporating the kinematic and constitutive relations:

$$
\begin{aligned}
\mathscr{E} &= \pi r \int_0^h \left[\varepsilon_z n_z + \varepsilon_\theta n_\theta + \kappa_z m_z \right] \, dz \\
&= \pi r \int_0^h \left[\varepsilon_z \left(C_{11}\varepsilon_z + C_{12}\varepsilon_\theta + C_{13}\kappa_z \right) + \varepsilon_\theta \left(C_{12}\varepsilon_z + C_{22}\varepsilon_\theta \right) + \kappa_z \left(C_{13}\varepsilon_z + C_{33}\kappa_z \right) \right] \, dz \\
&= \pi r \int_0^h \left[C_{11}\varepsilon_z^{\,2} + 2C_{12}\varepsilon_z\varepsilon_\theta + C_{22}\varepsilon_\theta^{\,2} + 2C_{13}\varepsilon_z\kappa_z + C_{33}\kappa_z^{\,2} \right] \, dz \\
&= \pi r \int_0^h \left[C_{11}\left(u'\right)^2 + 2C_{12}\left(w/r\right)u' + C_{22}\left(w/r\right)^2 + 2C_{13}\left(u'w''\right) + C_{33}\left(w''\right)^2 \right] \, dz
\end{aligned}
\tag{37}
$$

The 17×17 element stiffness matrix [**K**] is obtained after introducing Eq. (36) and its derivatives:

$$
\begin{aligned}
\mathscr{E} &= \{\mathbf{d}\}^{\mathrm{T}} \pi r \left\{ \int_0^h \begin{pmatrix}
 & C_{11} [\mathbf{T}_u]^{\mathrm{T}} \{\mathbf{G}'\}\{\mathbf{G}'\}^{\mathrm{T}} [\mathbf{T}_u] \\
+ & C_{12} \dfrac{1}{r}\left([\mathbf{T}_w]^{\mathrm{T}} \{\mathbf{G}\}\{\mathbf{G}'\}^{\mathrm{T}} [\mathbf{T}_u] + [\mathbf{T}_u]^{\mathrm{T}} \{\mathbf{G}'\}\{\mathbf{G}\}^{\mathrm{T}} [\mathbf{T}_w] \right) \\
+ & C_{22} \dfrac{1}{r^2} [\mathbf{T}_w]^{\mathrm{T}} \{\mathbf{G}\}\{\mathbf{G}\}^{\mathrm{T}} [\mathbf{T}_w] \\
+ & C_{13} \left([\mathbf{T}_u]^{\mathrm{T}} \{\mathbf{G}'\}\{\mathbf{G}''\}^{\mathrm{T}} [\mathbf{T}_w] + [\mathbf{T}_w]^{\mathrm{T}} \{\mathbf{G}''\}\{\mathbf{G}'\}^{\mathrm{T}} [\mathbf{T}_u] \right) \\
+ & C_{33} [\mathbf{T}_w]^{\mathrm{T}} \{\mathbf{G}''\}\{\mathbf{G}''\}^{\mathrm{T}} [\mathbf{T}_w]
\end{pmatrix} dz \right\} \{\mathbf{d}\} \\
&= \frac{1}{2} \{\mathbf{d}\}^{\mathrm{T}}_{1\times17} [\mathbf{K}]_{17\times17} \{\mathbf{d}\}_{17\times1}
\end{aligned}
\tag{38}
$$

Symmetry of the stiffness matrix in the presence of terms with C_{12} and C_{13} may be ensured by choosing the following expressions for the strains in terms of $\{\mathbf{G}\}$ and $\{\mathbf{d}\}$:

$$
\begin{aligned}
u'\frac{w}{r} &= \frac{1}{2}\left(\{\mathbf{d}\}^{\mathrm{T}} [\mathbf{T}_w]^{\mathrm{T}} \{\mathbf{G}\}\{\mathbf{G}'\}^{\mathrm{T}} [\mathbf{T}_u]\{\mathbf{d}\} + \{\mathbf{d}\}^{\mathrm{T}} [\mathbf{T}_u]^{\mathrm{T}} \{\mathbf{G}'\}\{\mathbf{G}\}^{\mathrm{T}} [\mathbf{T}_w]\{\mathbf{d}\} \right) \\
u'w'' &= \frac{1}{2}\left(\{\mathbf{d}\}^{\mathrm{T}} [\mathbf{T}_u]^{\mathrm{T}} \{\mathbf{G}'\}\{\mathbf{G}''\}^{\mathrm{T}} [\mathbf{T}_w]\{\mathbf{d}\} + \{\mathbf{d}\}^{\mathrm{T}} [\mathbf{T}_w]^{\mathrm{T}} \{\mathbf{G}''\}\{\mathbf{G}'\}^{\mathrm{T}} [\mathbf{T}_u]\{\mathbf{d}\} \right)
\end{aligned}
\tag{39}
$$

The stiffness terms of [**K**] evaluate to closed-form expressions requiring only the radius of the cylindrical element r, its meridional dimension h, the bending half-wavelengths (λ or α and β) and the stiffness terms of the constitutive relation. The number of unique terms is minimised due to the multiple symmetries featured by both membrane and bending shape functions.

4.5. Equivalent force vector from distributed load

The equivalent nodal force vector $\{\mathbf{f}\}$ may be obtained by considering the contributions to the total work W done by distributed element loads p_n and p_z, giving W_n and W_z respectively:

$$
W = \{\mathbf{d}\}^{\mathrm{T}} \{\mathbf{f}\} \quad \text{or} \quad W_n + W_z = \{\mathbf{d}\}^{\mathrm{T}} \left(\{\mathbf{f}_n\} + \{\mathbf{f}_z\} \right)
\tag{40}
$$

The known distributed loads may be expressed in vector form using interpolation functions L_1, L_2 and P (Table 1) in the following manner:

$$p_n = \{\mathbf{G}_p\}^{\mathrm{T}}_{1\times3}\{\mathbf{p}_n\}_{3\times1} \quad \text{and} \quad p_z = \{\mathbf{G}_p\}^{\mathrm{T}}_{1\times3}\{\mathbf{p}_z\}_{3\times1} \quad \text{where} \quad \{\mathbf{G}_p\} = \begin{Bmatrix} L_1 \\ L_2 \\ P \end{Bmatrix} \tag{41}$$

The $\{\mathbf{p}\}$ vectors are sampled from the known distributions of p_n and p_z at the nodes and at mid-height (Fig. 4), which keeps the load interpolation continuous between elements:

$$\begin{gathered} \{\mathbf{p}_n\} = \begin{Bmatrix} p_{n1} \\ p_{n2} \\ p_{n,mid} \end{Bmatrix} = \begin{Bmatrix} p_n(0) \\ p_n(h) \\ p_n(h/2) - \left[p_n(0) + p_n(h)\right]/2 \end{Bmatrix} \\ \text{and } \{\mathbf{p}_z\} = \begin{Bmatrix} p_{z1} \\ p_{z2} \\ p_{z,mid} \end{Bmatrix} = \begin{Bmatrix} p_z(0) \\ p_z(h) \\ p_z(h/2) - \left[p_z(0) + p_z(h)\right]/2 \end{Bmatrix} \end{gathered} \tag{42}$$

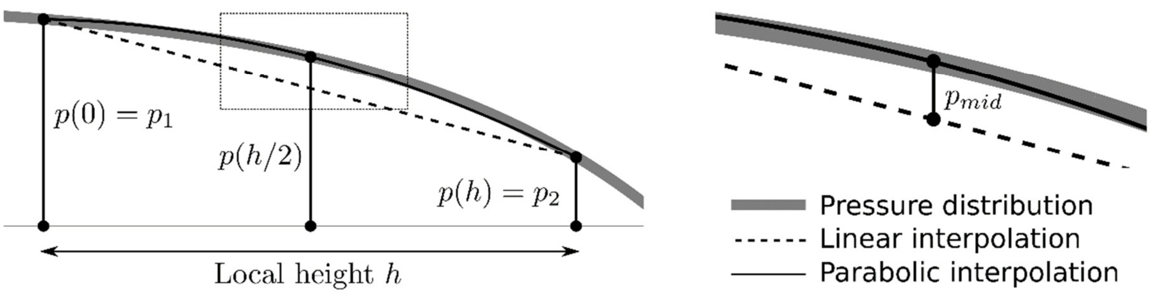

Fig. 4 – Distributed loading interpolation over an element

Using Eqs (36) and (41), it may be shown that:

$$\begin{gathered} W_n = 2\pi r\int_0^h p_n w\, dz = \{\mathbf{d}\}^{\mathrm{T}}_{1\times17} \underbrace{\left(2\pi r\int_0^h [\mathbf{T}_w]^{\mathrm{T}}_{17\times17}\{\mathbf{G}\}_{17\times1}\{\mathbf{G}_p\}^{\mathrm{T}}_{1\times3}\, dz\right)}_{[\mathbf{F}_n]_{17\times3}} \{\mathbf{p}_n\}_{3\times1} = \{\mathbf{d}\}^{\mathrm{T}}_{1\times17}\{\mathbf{f}_n\}_{17\times1} \\ W_z = 2\pi r\int_0^h p_z u\, dz = \{\mathbf{d}\}^{\mathrm{T}}_{1\times17} \underbrace{\left(2\pi r\int_0^h [\mathbf{T}_u]^{\mathrm{T}}_{17\times17}\{\mathbf{G}\}_{17\times1}\{\mathbf{G}_p\}^{\mathrm{T}}_{1\times3}\, dz\right)}_{[\mathbf{F}_z]_{17\times3}} \{\mathbf{p}_z\}_{3\times1} = \{\mathbf{d}\}^{\mathrm{T}}_{1\times17}\{\mathbf{f}_z\}_{17\times1} \end{gathered} \tag{43}$$

The terms of matrices $[\mathbf{F}_n]$ and $[\mathbf{F}_z]$ have a closed-form expression requiring only the radius r, dimension h and bending half-wavelengths (λ or α and β) and can therefore be used for multiple loads on the same structure without needing to be re-evaluated. These terms, and those of $[\mathbf{K}]$, may easily be derived by a symbolic manipulation package if desired by the reader.

4.6. Static condensation, assembly, nodal loads

Once the elements stiffness matrix [**K**] and element force vector {**f**} are obtained, static condensation can be performed on each to yield condensed stiffness matrices and force vectors. The process comes from the expression of the equilibrium equation reordered so that those related to nodal (index *no*) and element-specific (index *el*) DOFs are separated:

$$\begin{bmatrix} [\mathbf{K}_{no,no}]_{6\times6} & [\mathbf{K}_{no,el}]_{6\times11} \\ [\mathbf{K}_{el,no}]_{11\times6} & [\mathbf{K}_{el,el}]_{11\times11} \end{bmatrix} \begin{Bmatrix} \{\mathbf{d}_{no}\}_{6\times1} \\ \{\mathbf{d}_{el}\}_{11\times1} \end{Bmatrix} = \begin{Bmatrix} \{\mathbf{f}_{no}\}_{6\times1} \\ \{\mathbf{f}_{el}\}_{11\times1} \end{Bmatrix} \tag{44}$$

The second group of equation, relative to the element-specific DOFs, gives:

$$\{\mathbf{d}_{el}\}_{11\times1} = [\mathbf{K}_{el,el}]^{-1}_{11\times11} \left(\{\mathbf{f}_{el}\}_{11\times1} - [\mathbf{K}_{el,no}]_{11\times6} \{\mathbf{d}_{no}\}_{6\times1} \right) \tag{45}$$

Introducing Eq. (45) in the first group of equation, relative to the nodal DOFs, leads to:

$$[\mathbf{K}_{cond}]_{6\times6} \{\mathbf{d}_{no}\}_{6\times1} = [\mathbf{f}_{cond}]_{6\times1}$$

$$\text{where} \quad \begin{aligned} [\mathbf{K}_{cond}]_{6\times6} &= [\mathbf{K}_{no,no}]_{6\times6} - [\mathbf{K}_{no,el}]_{6\times11} [\mathbf{K}_{el,el}]^{-1}_{11\times11} [\mathbf{K}_{el,no}]_{11\times6} \\ \{\mathbf{f}_{cond}\}_{6\times1} &= \{\mathbf{f}_{no}\}_{6\times1} - [\mathbf{K}_{no,del}]_{6\times11} [\mathbf{K}_{el,el}]^{-1}_{11\times11} \{\mathbf{f}_{el}\}_{11\times1} \end{aligned} \tag{46}$$

The usual steps to assemble the global system can therefore be performed, the nodal DOFs being shared by elements sharing a node. For n elements, the matrix dimension is $3(n+1)$.

Lastly, the work done by an edge load at a node is the circumferential integral of the product of that edge load with the corresponding nodal displacement:

$$W_e = 2\pi r \left(q_z w + m_z \theta + n_z u \right) = \{\mathbf{d}_{node}\}^{\mathrm{T}}{}_{1\times3} \{\mathbf{f}_{node}\}_{3\times1}$$

The nodal force vectors can therefore be added to the assembled force vectors at the relevant position.

4.7. Boundary conditions and resolution

In order to prevent the overall translation of the shell in the meridional direction, at least one essential boundary condition (BC) on u is needed. Additional essential BCs can be enforced on u, w and θ at every node where no corresponding edge load (natural BC) is applied, using classical methods. The replacement of redundant equilibrium equations by the required BC equations is the one preferred here as it leaves the size of the linear system to be solved unchanged.

In any case, the nodal DOFs are obtained by solving the obtained linear system of equations, and for every element they can be used to retrieve the element-specific DOFs using Eq. (45). Finally, the values of the displacements, strains and stress resultants can be obtained at every point of each element from:

$$\begin{cases} w = \{\mathbf{G}\}^{\mathrm{T}}[\mathbf{T}_w]\{\mathbf{d}\} \\ \theta = \{\mathbf{G}'\}^{\mathrm{T}}[\mathbf{T}_w]\{\mathbf{d}\} \\ u = \{\mathbf{G}\}^{\mathrm{T}}[\mathbf{T}_u]\{\mathbf{d}\} \end{cases} \quad \text{and} \quad \begin{cases} \varepsilon_z = \{\mathbf{G}'\}^{\mathrm{T}}[\mathbf{T}_u]\{\mathbf{d}\} \\ \varepsilon_\theta = r^{-1}\{\mathbf{G}\}^{\mathrm{T}}[\mathbf{T}_w]\{\mathbf{d}\} \\ \kappa_z = \{\mathbf{G}''\}^{\mathrm{T}}[\mathbf{T}_w]\{\mathbf{d}\} \end{cases} \tag{47)(48}$$

$$\text{and} \quad \begin{cases} n_z = \left(C_{11}\{\mathbf{G}'\}^{\mathrm{T}}[\mathbf{T}_u] + C_{12}r^{-1}\{\mathbf{G}\}^{\mathrm{T}}[\mathbf{T}_w] + C_{13}\{\mathbf{G}''\}^{\mathrm{T}}[\mathbf{T}_w]\right)\{\mathbf{d}\} \\ n_\theta = \left(C_{12}\{\mathbf{G}'\}^{\mathrm{T}}[\mathbf{T}_u] + C_{22}r^{-1}\{\mathbf{G}\}^{\mathrm{T}}[\mathbf{T}_w]\right)\{\mathbf{d}\} \\ m_z = \left(C_{13}\{\mathbf{G}'\}^{\mathrm{T}}[\mathbf{T}_u] + C_{33}\{\mathbf{G}''\}^{\mathrm{T}}[\mathbf{T}_w]\right)\{\mathbf{d}\} \\ q_z = -\left(C_{13}\{\mathbf{G}''\}^{\mathrm{T}}[\mathbf{T}_u] + C_{33}\{\mathbf{G}'''\}^{\mathrm{T}}[\mathbf{T}_w]\right)\{\mathbf{d}\} \end{cases} \tag{49}$$

5. Illustration of the CSBL element on three examples

The performance of the CSBL element is illustrated here on three example problems, two of which are genuine practical design problems that require a non-trivial linear stress analysis of a multi-segment cylindrical metal shell. In each example, the CSBL element is compared against a 'classical' thin axisymmetric shell element (termed 'ThinAxi') using the formulation of Zienkiewicz *et al.* [11]. The latter relies on the same simple kinematic and constitutive relations introduced previously, but employs only simple polynomial shape functions: the four Hermite cubic functions N_1 to N_4 are used to interpolate w and θ, while the two linear functions L_1 and L_2 interpolate u. As there is no division into bending and membrane displacement components, system assembly can be done using shared DOFs yielding a stiffness matrix of size $3(n + 1)$ for n elements. The ThinAxi element thus represents a 'tried and tested' classical alternative, relying on low-order polynomials and h-refinement for convergence in the vicinity of the boundary layer. Both formulations were implemented using the Matlab [27] programming environment taking full advantage of matrix sparsity.

5.1. Example 1: single-thickness cylindrical shell under several loads

The first somewhat academic example is intended to illustrate the ability of a single CSBL element to exactly express a very rich displacement and stress state. A fictitious cylindrical shell of height $h = 2$ m, radius $r = 1$ m and uniform thickness $t = 10$ mm was considered, subject to a complete array of loading: linearly-varying outward normal pressure p_n from 0 at the top ($z = h$) to 1 MPa at the base ($z = 0$), linearly-varying downward meridional traction p_z from 0 at the top to 1 MPa at the base, and applied shell edge loads of $n_{zh} = 1000$ N/mm (downwards), $m_{zh} = 1000$ Nmm/mm (hogging) and $q_{zh} = 50$N/mm (radially outwards) at the unrestrained top boundary (Fig. 5a). The bottom boundary was restrained against all displacements and rotations ($w = u = 0$ and $\theta = 0$). An isotropic steel wall was assumed with elastic modulus $E = 200$ GPa and Poisson's ratio $\nu = 0.3$. The constitutive matrix and bending half-wavelengths thus become:

$$[\mathbf{C}] = \frac{1}{1-\nu^2}\begin{bmatrix} Et & \nu Et & 0 \\ \nu Et & Et & 0 \\ 0 & 0 & E\dfrac{t^3}{12} \end{bmatrix} \quad \text{thus } \lambda = \alpha = \beta = \pi\sqrt{rt}\left(\frac{1}{3(1-\nu^2)}\right)^{1/4} \approx 244.4\text{mm} \qquad (50)$$

This structure exhibits two bending boundary layers, each concentrated within approximately 2λ of either end, inside which a fine mesh resolution of classical ThinAxi elements is required (Fig. 5b). An often-applied rule of thumb is to use a *minimum* of 10 elements per λ within both of these regions to capture the high local curvatures reasonably well for practical purposes. By contrast, a significantly coarser mesh is usually sufficient for the purposes of a linear stress analysis within the internal 'membrane action' region: only 5 elements were used here. A total of 45 ThinAxi elements were thus generated requiring 135 DOFs, and it is stressed that this number is on the frugal side. Furthermore, it is clear that significant prior knowledge of cylindrical shell behaviour is required to be able to even design an appropriate mesh for this seemingly simple structure. By contrast, the design of a 'mesh' of CSBL elements is trivial (Fig. 5c), consisting of just the one element. Lastly, the problem is in fact simple enough to permit a closed-form analytical solution to the governing differential equation (Eq. (4)) for additional comparison.

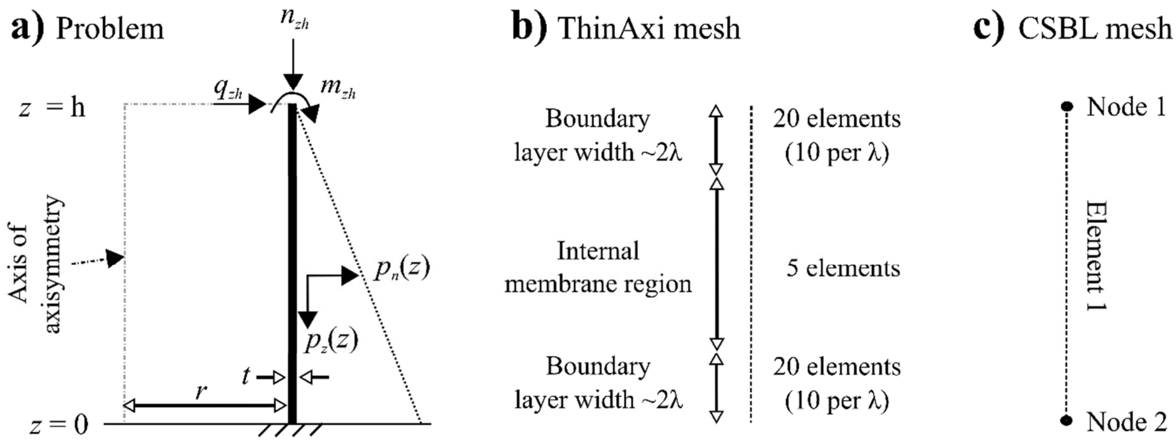

Fig. 5 – Geometry, loading and mesh design for the first example

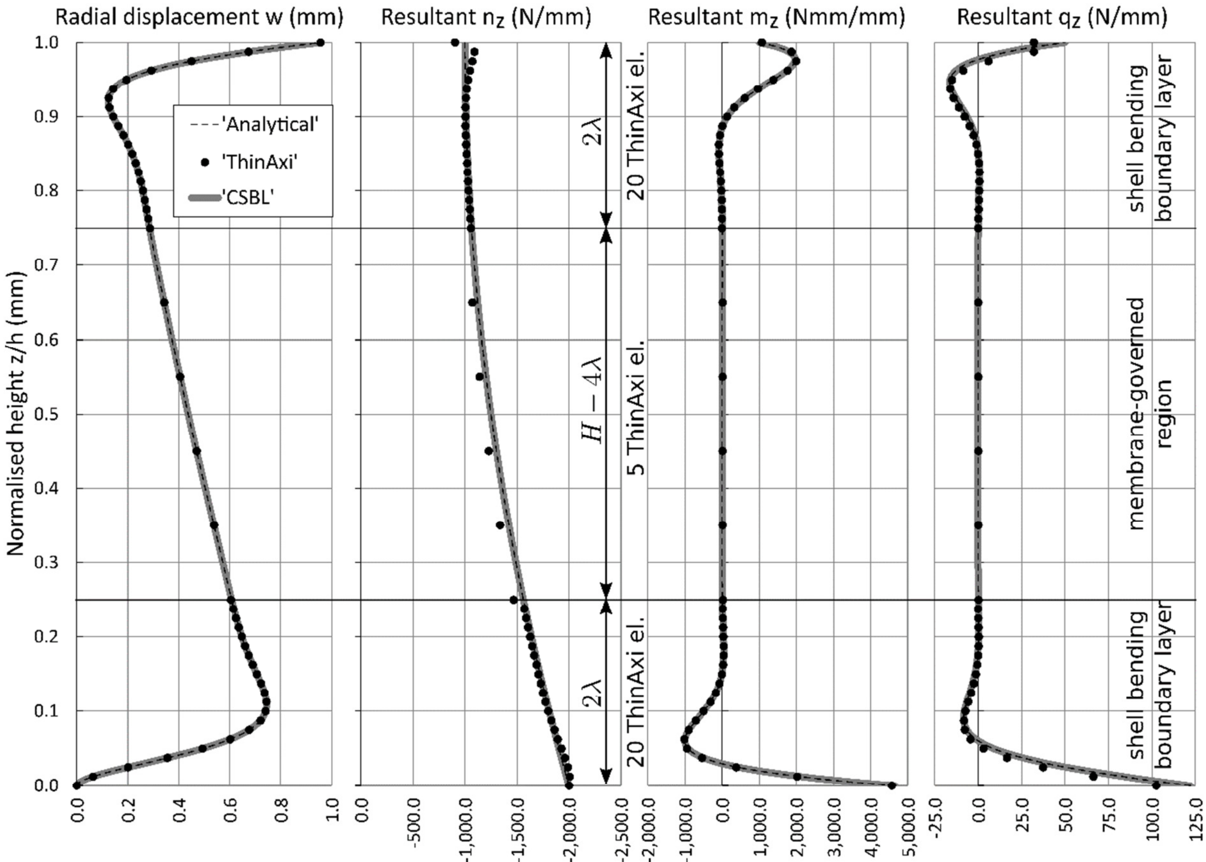

Fig. 6 – Comparison of predictions of the CSBL and ThinAxi elements for the first example

The global solutions for w, n_z, m_z and q_z are illustrated in Fig. 6. The compressive meridional membrane stress resultant n_z varies from -1000 N/mm at the top, where it is in equilibrium with the applied load n_{zh}, to -2000 N/mm at the base due to the downward action of p_z. The high rates of change of the total normal displacement w clearly illustrate the presence of a boundary layer within 2λ of either end, decaying onto an internal 'membrane' region with no bending where the displacement is proportional to p_n. This is further seen in the distribution of the meridional bending moment stress resultant m_z, which is non-zero only in the boundary layer and zero in the internal region.

The agreement between the predictions of the ThinAxi element and the analytical solution is very close for w (0.84 % max normalised error), unsurprising given that it is a nodal variable, but becomes increasingly less satisfactory for derived higher-order stress variables (4.8 %, 2.6 % and 16 % max norm. error respectively for n_z, m_z and q_z). Eq. (18) suggests that u is also affected by the boundary layer, albeit to a smaller extent than w, a behaviour that the classical ThinAxi formulation is ill-prepared to capture as it uses only a linear interpolation for u. Further mesh refinement is necessary within the boundary layers to alleviate this, exacerbating the DOF cost for the ThinAxi element. By contrast, the single CSBL element exhibits no such limitation, reproducing the numerical predictions of the analytical solution exactly (10^{-14} % max norm. error over all variables, close to machine precision), at a cost of only 17 DOFs. In terms of system assembly and solution time, the CSBL is also 6 % faster on average over 100 runs. The rather modest speedup for this small problem should be understood in the context of the higher *flop* cost in computing the more complex expressions for the coefficients of the stiffness matrix of the CSBL element.

5.2. Example 2: isotropic silos with stepwise-varying thickness under nonlinear loading

The second example is intended to illustrate the effectiveness of an assembly of CSBL elements to perform an accurate and efficient linear stress analysis of a multi-strake cylindrical shell under nonlinear distributed pressure loads. To this end, five realistic stepped-wall cylindrical metal silos were modelled using meshes of both ThinAxi and CSBL elements. The silos differ in total height to diameter H/D ratio but share a common storage volume of ~510 m^3 and exhibit stepwise-increasing integer wall thickness distributions with depth (Fig. 7), as is common in engineering practice. The silos are denoted as VS (H/D = 5.2), S (H/D = 3), B (H/D = 2.06), I (H/D = 1.47) and Q (H/D = 0.65). The structural designs were performed on the basis of membrane theory according to EN 1993-1-6 and EN 1993-4-1 [28, 29] with loading given by EN 1991-4 [30]. The interested reader may find full details of the design, loading and further discussion in [31].

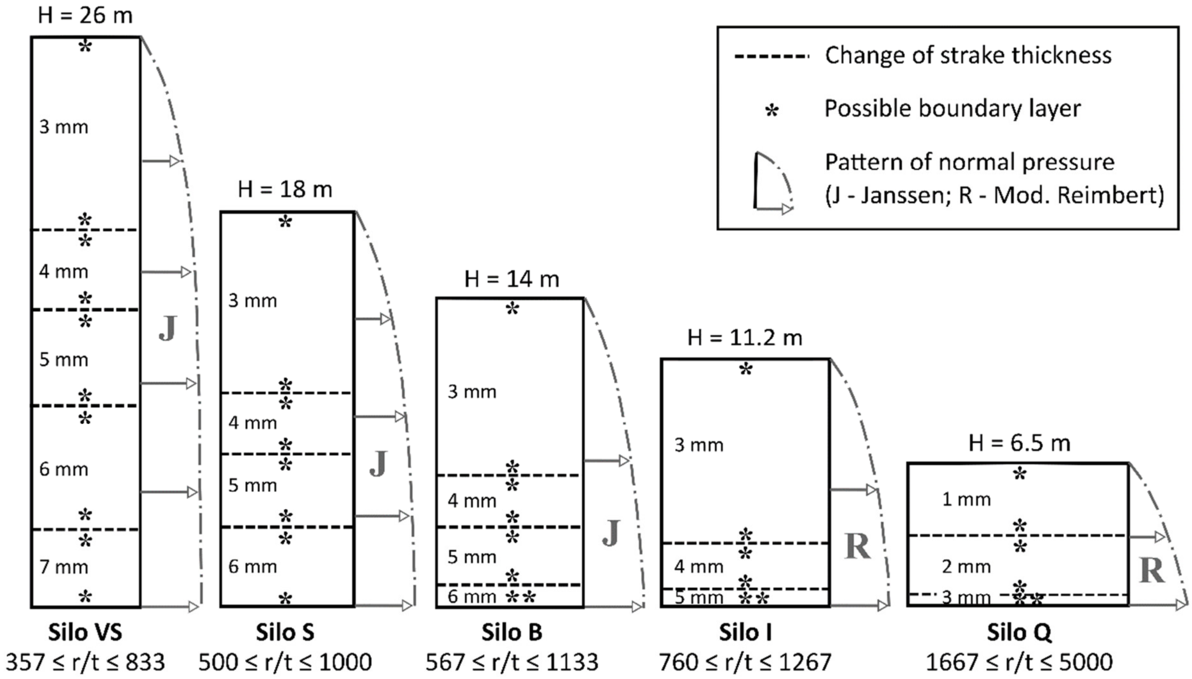

Fig. 7 – Geometry (shown to scale) and loading of the five silos for the second example

The silos store a granular solid (wheat) which exerts a nonlinear normal pressure p_n that increases monotonically to an asymptotic limit with depth, as well as associated frictional tractions p_z that follow the same distribution. For the three most slender silos (VS, S and B), the variation with z is negative exponential and is known as a 'Janssen' distribution, while for the squattest silos (I and Q) the variation follows a power law instead and is known as a 'modified Reimbert' distribution [26]. The outline patterns of these distributions, all actually quite similar, are also illustrated in Fig. 7. While nonlinear, the distributions are very smooth, and can be very well approximated in a piecewise quadratic manner.

The silos are assumed to be fully restrained at the base ($w = u = 0$ and $\theta = 0$). At the top, only the normal displacement w is restrained, a boundary condition assumedly provided by a roof structure. An isotropic steel material is assumed throughout with $E = 200$ GPa and $\nu = 0.3$ (Eq. (50)). As the radii and thicknesses vary across the silo designs, each wall strake exhibits a different bending half-wavelength λ (Table 2). Further, every internal step change in wall thickness represents a discontinuity in the membrane displacements and thus leads to compatibility bending with an associated boundary layer on either side (marked * in Fig. 7), the rate of decay of which is governed by the λ of the strake in which it occurs. Silo VS potentially exhibits 10 boundary layers, while silos S, B, I and Q may exhibit 8, 8, 6 and 6 respectively: the structures are therefore too complex to allow for a closed-form analytical bending theory solution, and finite elements are needed even for a linear stress analysis.

Accordingly, modelling each silo with ThinAxi elements requires careful planning, as a fine mesh must be used within 2λ on either side of every discontinuity to accommodate the boundary layers. The simple rule of thumb of a minimum of 10 elements per λ signals the possibility of a high DOF count, and a mesh convergence study is often necessary for optimality. Where the mesh is to be partitioned in this manner prior to analysis, each λ must usually be calculated manually by the analyst from standard expressions, a laborious task. By contrast, mesh design for the CSBL element requires significantly less effort, as a single such element can automatically be assigned to a strake, with λ being treated as just another coefficient to be computed 'internally' during stiffness matrix assembly. Strake boundaries then represent the nodes of CSBL elements.

Table 2 – Details of strake thicknesses t, depths h and aspect ratios h/λ for the five silos

Silo VS r = 2500 †			Silo S r = 3000			Silo B r = 3400			Silo I r = 3800			Silo Q r = 5000		
t †	h†	h/λ ‡	t	h	h/λ	t	h	h/λ	t	h	h/λ	t	h	h/λ
3	8800	41.6												
4	3600	14.7	3	8200	35.4	3	8000	32.4						
5	4400	16.1	4	2800	10.5	4	2400	8.4	3	8200	31.4	1	3300	19.1
6	5600	18.7	5	3200	10.7	5	2600	8.2	4	2200	7.3	2	2700	11.1
7	3600	11.1	6	3800	11.6	6	1000	2.9	5	800	2.4	3	500	1.7

Note: † dimensions in mm; ‡ dimensionless.

The predictions of the ThinAxi and CSBL element models for the normal displacement w and the meridional stresses σ_z on the inner and outer shell surfaces are shown in Fig. 8, together with element and DOF counts for each mesh and silo. The data have been scaled to separate out the plots for enhanced readability, with scaling factors given in the legend for that figure. The differences between the ThinAxi and CSBL models results, normalised by the maximum absolute value of the considered field, were computed for every interpolation point and their 95th percentile over each boundary layer and membrane-governed region are shown at the middle of the corresponding regions for the most and least slender silos VS and Q respectively.

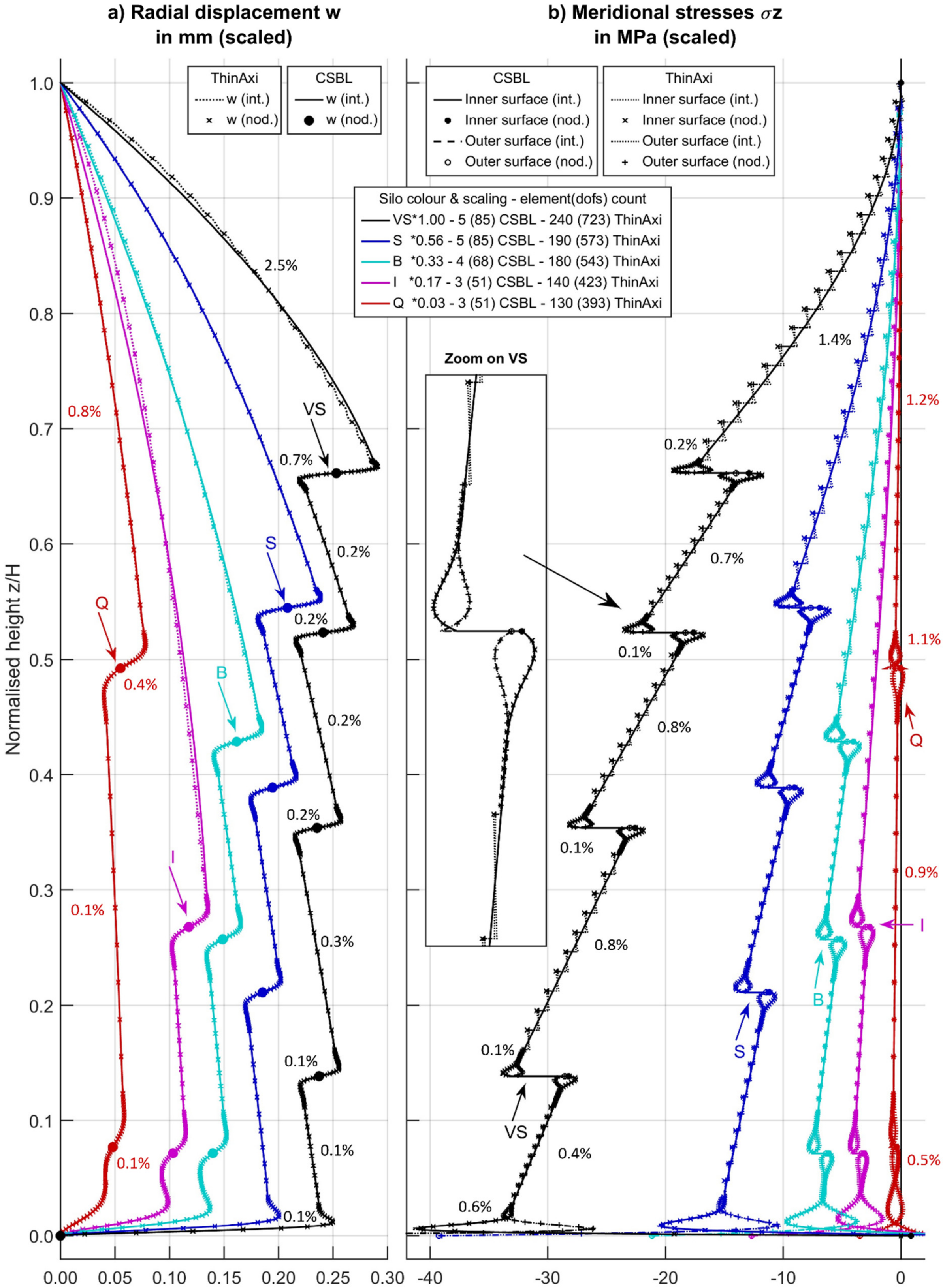

Fig. 8 – a) Normal displacement w and b) meridional surface stresses σ_z obtained with the CSBL and ThinAxi elements.

Note: the data have been scaled for readability – scaling factors may be found in the legend.

The agreement between the two models is excellent, with the CSBL mesh requiring only 40 % of the DOFs of an optimised ThinAxi mesh. Both solutions hint at a discontinuity in w at every change of thickness, and clearly show the localised boundary layers of compatibility bending (w_b) necessary to force the solution to be continuous from one membrane particular integral (w_m) to another. The associated higher local stresses are rather modest except at the base of each silo, where very high surface stresses develop. The error due to the piecewise-parabolic approximation of the load is noticeable only in the upper part of the silos where the distributions exhibit the highest gradients, and remains very reasonable due to the smooth nature of silo loadings. In terms of computation time, the CSBL models are between 6 and 17 % faster than their ThinAxi counterparts (when comparing average runtimes for system assembly and solution out of 50 repeat calculations).

5.3. Example 3: meridionally-stiffened corrugated shell with stepwise-varying thickness

The final example extends on the second to illustrate the effectiveness of an assembly of CSBL elements to model a complex multi-strake silo with circumferentially corrugated metal walls and meridional stiffeners, both of which exhibit a stepwise variation in thickness, using a 'smeared' stiffness approach [23, 24]. The solution is compared against an assembly of ThinAxi elements, as well as a detailed 3D model built using the commercial ABAQUS 6.14-4 [32] software which explicitly considers the corrugation and stiffener profiles to validate the axisymmetric 'smeared' stiffness assumption.

Corrugations and meridional stiffeners are a common feature of silo design: the corrugations greatly enhance the circumferential bending stiffness of the shell though at a significant penalty to the meridional stiffness so that axial loads must instead be carried almost entirely by external columns [22, 26]. The present example considers a real design, carried out according to NF P 22-630 [33] and DIN 1055-6 [34], of a wheat silo of nominal radius $r = 8.885$ m built with 12 corrugated strakes of equal height $h = 1.144$ m up to a total height $H = 13.728$ m (Fig. 9a). The corrugated sheets have a thickness varying from 1.5 to 2.5 mm with an 'arc and tangent' profile (Fig. 9b). There are 60 external column stiffeners with varying Ω profiles, bolted to the external peaks of the corrugations, with a spacing of $d_{st} = 933$ mm (Fig. 9c). Both the strakes and stiffeners are made of isotropic steel with $E = 200$ GPa and $\nu = 0.3$. The present analyses assume a smooth but nonlinear axisymmetric 'Janssen' pressure distribution for the stored wheat using material properties from EN 1991-4 [30], with additional provisions for corrugated silos from EN 1993-4-1 [28, 29].

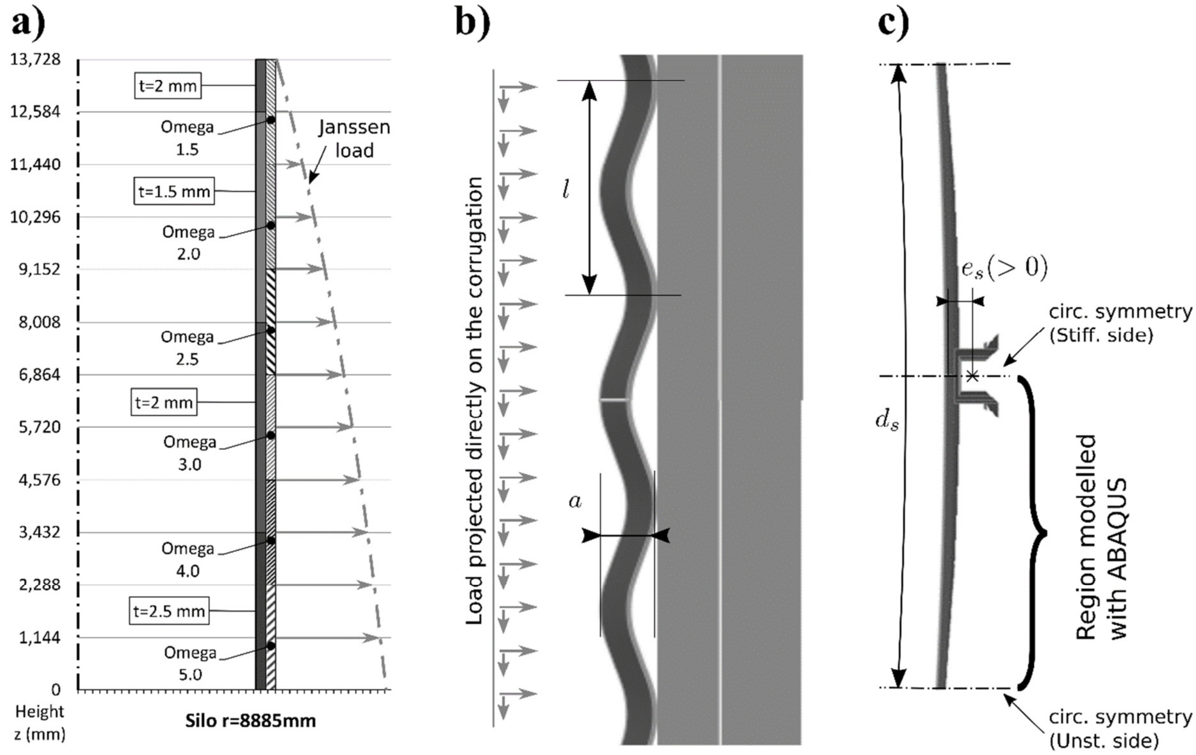

Fig. 9 – Overall geometry, shell-thickness and stringer distribution of the silo for the third example a), corrugation profile b) and stiffener positioning c)

The ABAQUS reference model uses a combination of linear four-node reduced-integration S4R shell and linear two-node B21 beam elements to accurately model the corrugated shell and the stiffeners respectively. The meridional corrugation profile (Fig. 9b) can be expressed well by 28 S4R elements per corrugation wave (approx. element size of 5 mm). Circumferential symmetry is exploited to model the smallest possible arc of the shell (Fig. 9c). As important variations can also be expected in that direction, 47 S4R elements (approx. size 20 mm) were used, which helps to maintain a reasonable aspect ratio for the shell elements. With 11 waves in every of the 12 strakes, a total of 173,712 shell elements were required. While it is probably possible to optimise the element count, doing so is unlikely to lead to a significant reduction in the required number of total elements.

The stiffeners were modelled using 22 B21 elements per strake, up to a total of 264. Connector elements CON3D2 were used to link the beam and shell element DOFs at each of the 132 contact points. Boundary conditions were assumed the same as in the second example: clamped base and restrained normal displacement at the top. For simplicity, the distributed pressure and friction tractions loads were assumed to act in the radial and meridional directions regardless of local incline of the corrugated wall (Fig. 9b), an assumption that is implicitly made with the ThinAxi and CSBL models. It should be noted that building the complex geometry of such a model demands significant skill on the part of the analyst, with extensive use of Python scripting.

The use of axisymmetric shell elements is possible with the help of the 'smeared' stiffness approach. This treats the silo as a composite cylindrical shell with a uniformly orthotropic stiffness that is a superposition of two cylinders with equivalent membrane and bending stiffnesses corresponding to the corrugated shell [$\mathbf{C}_{shell}$] and stiffeners [$\mathbf{C}_{stiffeners}$] respectively. The constitutive relation is thus:

$$\begin{Bmatrix} n_z \\ n_\theta \\ m_z \end{Bmatrix} = \left(\left[\mathbf{C}_{shell}\right] + \left[\mathbf{C}_{stiffeners}\right]\right) \begin{Bmatrix} \varepsilon_z \\ \varepsilon_\theta \\ \kappa_z \end{Bmatrix} \tag{51}$$

The equivalent orthotropic properties for a corrugated shell can be found in EN 1993-4-1 [29] as follows (a and l are defined in Fig. 9b):

$$\left[\mathbf{C}_{shell}\right] = \begin{bmatrix} C_{11,sh} & 0 & 0 \\ 0 & C_{22,sh} & 0 \\ 0 & 0 & C_{33,sh} \end{bmatrix} \tag{52}$$

where $C_{11,sh} = E\dfrac{2t^3}{3a^2}$, $C_{22,sh} = Et\left(1+\dfrac{\pi^2 a^2}{4l^2}\right)$ and $C_{33,sh} = \dfrac{Et^3}{12\left(1-\nu^2\right)} \cdot \left(1+\dfrac{\pi^2 a^2}{4l^2}\right)^{-1}$

It may be noted that these properties ignore Poisson coupling in the meridional and circumferential directions, and that the circumferential membrane stiffness $C_{22,sh}$ is significantly greater than the meridional membrane stiffness $C_{11,sh}$. EN 1993-4-1 [29] additionally specifies that stiffener spacing d_{st} of 933 mm should be less than a maximum value $d_{st,max}$ to validate a 'smeared' treatment. This criterion is met, with the limit given by:

$$d_{st,\max} = 7.4\left(\frac{r^2\left(0.13Eta^2\right)}{C_{22,sh}}\right)^{0.25} = 1439 \text{ mm} \tag{53}$$

Lastly, displacements, strains and stress resultants in the shell are obtained using Eqs (47)-(49) with the relevant [$\mathbf{C}_{shell}$] terms.

The contribution of the stiffeners, expressed with respect to the midsurface of the orthotropic shell, depends on their material (E_{st}) and section (A_{st} and I_{st}) properties, and their eccentricity relative to the cylinder (e_{st}) and spacing (d_{st}) [22, 29]:

$$\left[\mathbf{C}_{stiffeners}\right]=\begin{bmatrix} \dfrac{E_{st}A_{st}}{d_{st}} & 0 & \dfrac{e_{st}E_{st}A_{st}}{d_{st}} \\ 0 & 0 & 0 \\ \dfrac{e_{st}E_{st}A_{st}}{d_{st}} & 0 & \dfrac{E_{st}I_{st}}{d_{st}}+\dfrac{e_{st}^{\,2}E_{st}A_{st}}{d_{st}} \end{bmatrix} \tag{54}$$

The resultant axial force N_z and bending moment M_z in the beam sections, with respect to the centroid of the stiffener, may be obtained by:

$$\begin{Bmatrix} N_z \\ M_z \end{Bmatrix}=\begin{bmatrix} E_{st}A_{st} & e_{st}E_{st}A_{st} \\ 0 & E_{st}I_{st} \end{bmatrix}\begin{Bmatrix} \varepsilon_z \\ \kappa_z \end{Bmatrix} \tag{55}$$

The columns exhibit a meridional bending stiffness far greater than that of the shell itself, and the resulting bending half-wavelengths $\alpha \neq \beta$ are of the same order as the strake dimensions. The bending boundary layer thus dominates the entire structure, and a simple conventional stress analysis based solely on membrane equilibrium would be entirely inappropriate [22]. A full bending analysis is necessary even to obtain the linear stress state, and since the multi-strake structure is much too complex for a closed-form analytical solution this must be done with finite elements. It is interesting to note that just a single ThinAxi element per strake will in fact give a reasonably good solution for the normal displacement w in the 'smeared' shell, since in the limit $H/\alpha \rightarrow 0$ the boundary layer shape functions anyway converge to the Hermite cubic polynomials that the ThinAxi element uses to interpolate w (Fig. 2). However, the solution for the meridional displacement would be very inadequate in this case due to that element's linear interpolation field for u. Each 'smeared' strake was therefore modelled with 10 ThinAxi elements (the rule of the thumb of 10 elements per bending half-wavelength now being redundant) to solve for both w and u more accurately, up to a total of 120. By contrast, only a single CSBL element was necessary per strake, up to a total of 12. The modelling effort required in either case is trivial compared with the complexity of creating a 3D model. The element, node and DOF counts in the three models are compared in Table 3.

Table 3 – Comparison of the complexities of the finite element models

Model	No. of elements	No. of nodes	No. of DOFs
ABAQUS	178,704†	183,156	1,098,144‡
ThinAxi	120	121	363
CSBL	12	13	204

† includes both shell and beam elements; ‡ includes Lagrange multipliers

A very good agreement is observed between the three finite element models for the solution governing the stiffeners (Fig. 10), with the ThinAxi and CSBL predicting a very similar response. Using ABAQUS as the reference solution, 90 % of the sampled ThinAxi and CSBL predictions exhibit a relative error below 6.2, 6.6 and 15 % for the transverse displacement *w*, axial displacements *u* and the axial force N_z respectively. The axial force increases monotonically with depth to a maximum compressive value of ~175kN near the base where the risk of buckling is thus greatest, while the bending moment is negligible everywhere except near the base where it peaks at ~6 kNm. The relative error in N_z and M_z in the lowest strake is less than 20 % and 30 % respectively, the discrepancy being a consequence of the 'smeared' stiffness approach rather than the choice of interpolation field for either the CSBL or ThinAxi elements. Similarly, the agreement between the three models for the solution within the shell itself is satisfactory (Fig. 11, where the ThinAxi solution is not represented for readability as it does not differ significantly from that of the CSBL). The normal displacements *w* of the shell were extracted from the ABAQUS model at the stiffened and unstiffened locations (Fig. 9c). On the stiffened side, the shell displacements closely follow those of the stiffener (Fig. 10), while on the unstiffened side the displacements are larger due to the increased local flexibility.

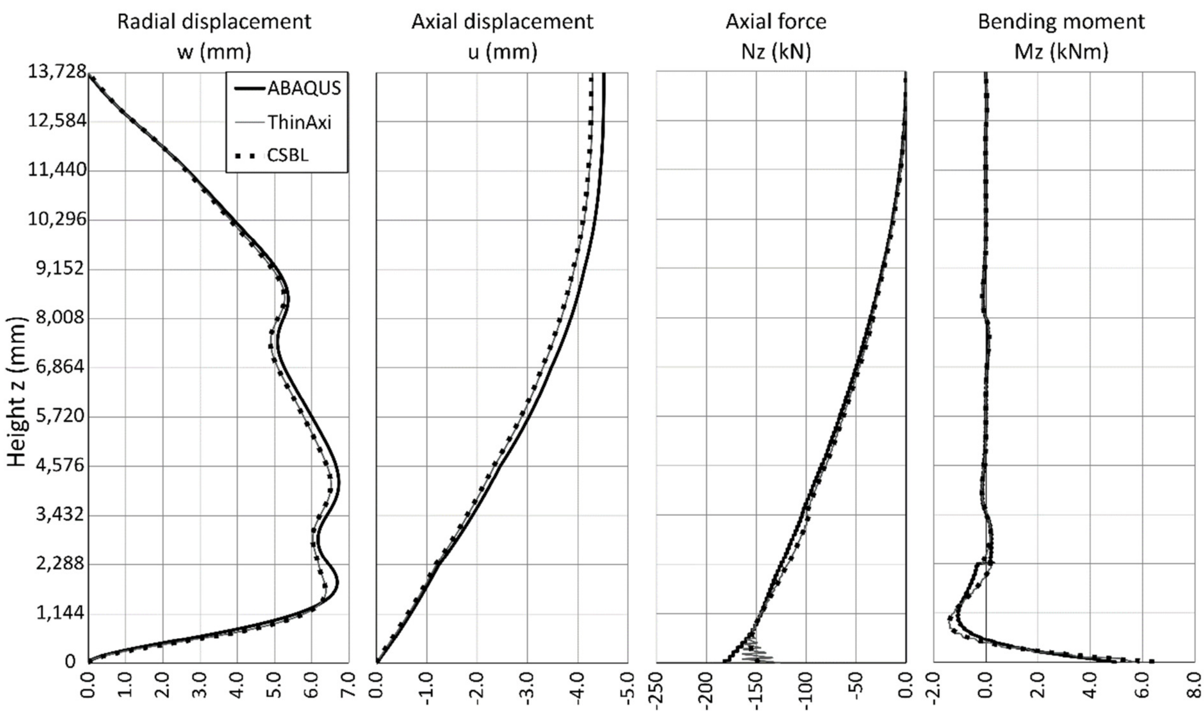

Fig. 10 – Transverse and axial displacements, force and bending moment for the stiffeners obtained with the ABAQUS, ThinAxi and CSBL finite element models

Also shown in Fig. 11 are the circumferential σ_θ and meridional σ_z stresses on the inner shell surface. As the actual stresses in the ABAQUS model follow the corrugation profile and feature important oscillations, a moving average with a period fitted to the wavelength of the corrugation is used to enable an easier comparison and better readability. The CSBL results are globally in excellent agreement with ABAQUS, with the exception of the bottom boundary and near changes of corrugation (but not stiffener) thickness. This is due to significant non-axisymmetric bending that occurs at those locations that is strongly dependent on the exact manner in which they are modelled in ABAQUS, but which it is anyway not possible to reproduce through a 'smeared stiffener' treatment. The largest error is observed for the shell meridional stresses on the unstiffened side in the bottom strake, since the stresses developed there are underestimated by an order of magnitude by the 'smeared' stiffness model. A reduction in the stiffener circumferential spacing d_s would improve the quality of the results for the unstiffened side, as it would make the problem closer to axisymmetric. The 'smeared' approach is, however, clearly a very valuable simplifying design tool for certain structures, and the CSBL implementation is preferable over a classical shell formulation as it captures the higher order variables (stresses and resultants) more accurately with fewer DOFs and requires significantly less modelling effort.

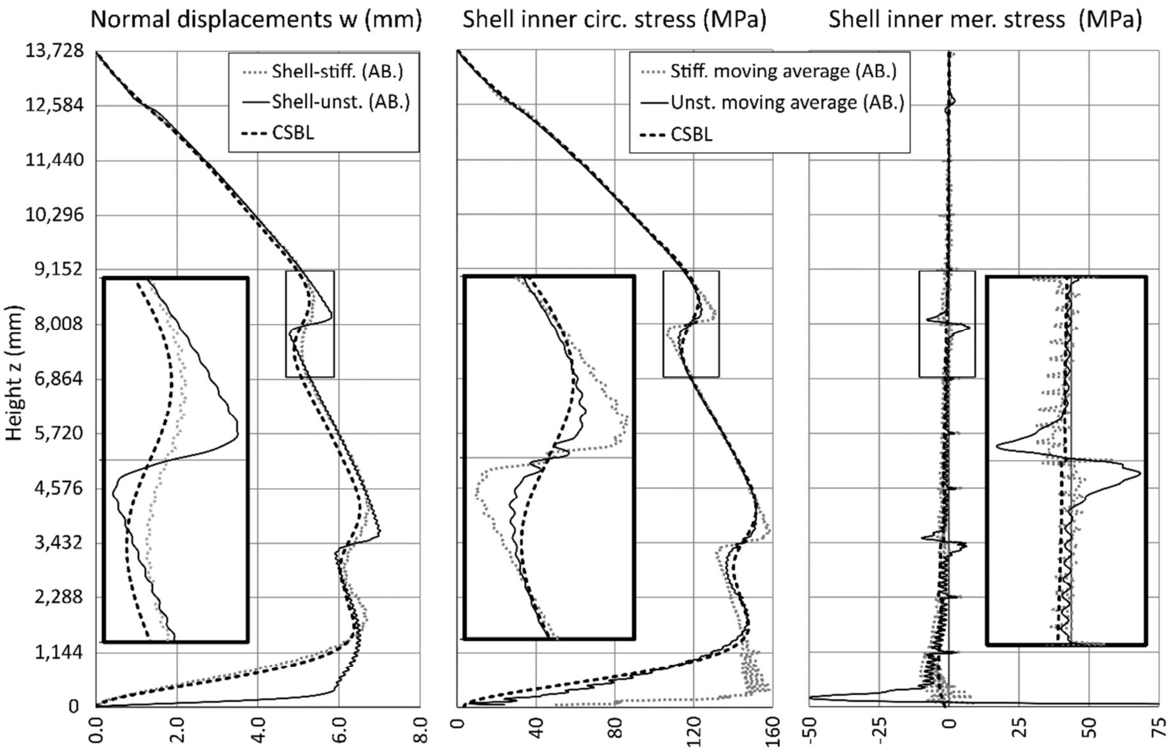

Fig. 11 – Normal displacements, inner circumferential and meridional surface shell stresses obtained with ABAQUS and the CSBL finite element models

6. Conclusions and further development

This 'proof of concept' paper builds on an axisymmetric bending theory for thin orthotropic cylindrical shells presented in [22] to develop a novel cylindrical shell boundary layer (CSBL) finite element. Specialised shape functions are introduced to enrich the element to exactly capture the 'boundary layer' of local bending that occurs near supports, changes of wall thickness and other discontinuities. These shape functions are obtained directly from the solution to the governing differential equation and permit the interpolation of the bending components of the nodal displacement variables separately from the membrane components.

The proposed formulation permits just a single CSBL element to exactly capture the stresses and displacements of an entire cylindrical shell under up to second order polynomial distributed loading. The ability of the element to accurately and efficiently analyse more realistic design problems, featuring more complex loads and geometries, multi-segment cylindrical strakes with stepwise-varying wall thickness and meridional stiffener distributions was demonstrated on three examples of increasing complexity and practical relevance. For two of these, even a linear bending stress analysis is prohibitively onerous analytically.

Comparisons with classical axisymmetric shell elements based on low-order polynomial shape functions and the commercial ABAQUS software show that the added complexity of the CSBL formulation may be balanced by a significantly simpler meshing and modelling procedure. Additionally, the CSBL element leads to a system with a lower number of degrees of freedom and faster runtimes than an alternative classical axisymmetric shell formulation.

Under linear conditions, the rate of decay of the bending boundary layer is governed by the bending half-wavelength, a quantity always known *a priori* for any cylindrical shell from standard expressions that is coded into the proposed bending shape functions. However, under geometrically nonlinear conditions, the bending half-wavelength is known to be greatly amplified by the level of local meridional stress, but the only known closed-form expression for the nonlinear bending half-wavelength relates to a cylinder under uniform meridional compression [35]. Ongoing development on a nonlinear axisymmetric CSBL element aims to implement the bending half-wavelength as an element DOF, with only *initial* values given by linear expressions. Additionally, the formulation is currently being extended to other shells of revolution and Gaussian curvatures, including cones and spheres which exhibit significantly wider boundary layers than cylinders, as well as non-axisymmetric conditions and different sets of practical boundary conditions such as stiffening rings and elastic foundations.

7. Acknowledgements

The authors are very grateful to Leopold Sokol of Sokol-Palisson Consultants in France for kindly providing details of the silo design used in one of the examples shown in this study. The research was made possible thanks to a Skempton Scholarship kindly awarded by the Department of Civil and Environmental Engineering of Imperial College London.

8. References

[1] Rotter J. Membrane theory of shells for bins and silos. Trans.Mech.Engng, IE Australia 1987:135-47.

[2] Rotter J. Bending theory of shells for bins and silos. Trans.of Mech.Eng 1987:264-71.

[3] Koiter W. A consistent first approximation in the general theory of thin elastic shells. Theory of Thin Elastic Shells 1960:12-33.

[4] Novozhilov VV. The theory of thin shells: P. Noordhoff, 1959.

[5] Budiansky B, Sanders JL. On the "best" first-order linear shell theory, Cambridge, Mass.: Division of Engineering and Applied Physics, Harvard University, 1962.

[6] Flügge W. Stresses in shells, Germany: Springer-Verlag Berlin-Heidelberg, 1973.

[7] Timoshenko, Stephen & Woinowsky-Krieger, S. Theory of plates and shells, New York: McGraw-Hill, 1987.

[8] Khelil A, Belhouchet Z, Roth JC. Analysis of elastic behaviour of steel shell subjected to silo loads. Journal of Constructional Steel Research 2001;57:959-69.

[9] Rutten HS. Theory and design of shells on the basis of asymptotic analysis: Rutten and Kruisman, 1973.

[10] Baker EH, Kovalevsky L, Rish F. Structural analysis of shells: Krieger Publishing Company, 1981.

[11] Zienkiewicz OC, Taylor RL, Fox DD. The finite element method for solid and structural mechanics, Oxford; Waltham, Mass.: Butterworth-Heinemann, 2014.

[12] Zienkiewicz OC, Taylor RL, Zhu JZ. The Finite Element Method: Its Basis and Fundamentals, Jordon Hill: Elsevier Science, 2014.

[13] Cook RD. Concepts and applications of finite element analysis: Wiley, 1981.

[14] Zienkiewicz OC, De S.R. Gago JP, Kelly DW. The hierarchical concept in finite element analysis. Comput Struct 1983;16:53-65.

[15] Chapelle D, Bathe K. The Finite Element Analysis of Shells - Fundamentals, Berlin, Heidelberg: Springer Berlin Heidelberg, 2010.

[16] Rotter JM, Sadowski AJ, Chen L. Nonlinear stability of thin elastic cylinders of different length under global bending. Int J Solids Structures 2014;51:2826-39.

[17] Melenk JM, Babuška I. The partition of unity finite element method: Basic theory and applications. Comput Methods Appl Mech Eng 1996;139:289-314.

[18] Moës N, Dolbow J, Belytschko T. A finite element method for crack growth without remeshing. Int J Numer Methods Eng 1999;46:131-50.

[19] Alves PD, Barros FB, Pitangueira RLS. An object-oriented approach to the Generalized Finite Element Method. Adv Eng Software 2013;59:1-18.

[20] Jeon H, Lee P, Bathe K. The MITC3 shell finite element enriched by interpolation covers. Comput Struct 2014;134:128-42.

[21] Love AEH. The Small Free Vibrations and Deformation of a Thin Elastic Shell. Philosophical Transactions of the Royal Society of London.A 1888;179:491-546.

[22] Rotter JM, Sadowski AJ. Cylindrical shell bending theory for orthotropic shells under general axisymmetric pressure distributions. Eng Struct 2012;42:258-65.

[23] Baruch M, Singer J. Effect of eccentricity of stiffeners on the general instability of stiffened cylindrical shells under hydrostatic pressure. Journal of Mechanical Engineering Science 1963;5:23-7.

[24] Singer J. The influence of stiffener geometry and spacing on the buckling of axially compressed cylindrical and conical shells (extended version) 1967;TAE Reports 68, Department of Aeronautical Engineering, Technion, Haifa, Israel.

[25] Babuška I, Guo BQ. The h, p and h-p version of the finite element method; basis theory and applications. Adv Eng Software 1992;15:159-74.

[26] Rotter JM. Guide for the economic design of circular metal silos: CRC Press, 2001.

[27] The MathWorks Inc. MATLAB R2015b.

[28] EN 1993-1-6:2007. Eurocode 3, design of steel structures, Part 1-6: strength and stability of shell structures, London: Comité Européen de Normalisation, Brussels, 2007.

[29] EN 1993-4-1:2007. Eurocode 3, design of steel structures, Part 4-1: silos: Comité Européen de Normalisation, Brussels, 2007.

[30] EN 1991-4-1:2006. Eurocode 1, actions on structures, Part 4: silos and tanks.: Comité Européen de Normalisation, Brussels, 2006.

[31] Sadowski AJ, Rotter JM. Steel silos with different aspect ratios: I — Behaviour under concentric discharge. Journal of Constructional Steel Research 2011;67:1537-44.

[32] Dassault Systèmes Simulia Corp. ABAQUS 2014;6.14.

[33] NF P22-630:Jan. 1992. Construction métallique - Silos en acier - Calcul des actions dans les cellules: AFNOR, 1992.

[34] DIN 1055-6:2005-03. Enwirkungen auf Tragwerker - Teil 6: Enwirkungen auf Silos und Flüssigkeitsbehälter: Beuth Verlag, 2005.

[35] Rotter JM, University of Sydney. School of Civil, Mining Engineering. Stress amplification in unstiffened steel silos and tanks 1983.